CryoET Reveals Organelle Phenotypes in Huntington Disease Patient iPSC-Derived and Mouse Primary Neurons

Wah Chiu (✉ wahc@stanford.edu)
   Stanford University   https://orcid.org/0000-0002-8910-3078

Gong-her Wu
   Stanford University

Jesús Galaz-Montoya
   Stanford University

Michael Schmid
   Stanford University   https://orcid.org/0000-0003-1077-5750

Lydia Joubert
   Stanford University   https://orcid.org/0000-0002-4709-007X

Patrick Mitchell
   SLAC National Accelerator Laboratory   https://orcid.org/0000-0002-3458-6930

Cristina Danita
   Stanford University

Serena Yeung
   Stanford University   https://orcid.org/0000-0003-0529-0628

Sanket Gupte
   Stanford University

Joy Hsu
   Stanford University   https://orcid.org/0000-0001-9023-4940

Judith Frydman
   Stanford University   https://orcid.org/0000-0003-2302-6943

Ranen Aviner
   Stanford University

William Mobley
   University of California, San diego

Chengbiao Wu
   University of California, San diego

Yingli Gu
   UCSD School of Medicine

Charlene Smith-Geater

University of California, Irvine   https://orcid.org/0000-0003-2136-4420

Leslie Thompson
  University of Caliornia, Irvine

Ricardo Miramontes
  University of California, Irvine

Keona Wang
  University of California, Irvine

Nicolette Geller
  University of California, Irvine

Article

CryoET Reveals Organelle Phenotypes in Huntington Disease Patient iPSC-Derived and Mouse Primary Neurons

Gong-Her Wu[1,*], Charlene Smith-Geater[2,*], Jesús G. Galaz-Montoya[1], Yingli Gu[3], Sanket R. Gupte[4], Ranen Aviner[5], Patrick G. Mitchell[6], Joy Hsu[4], Ricardo Miramontes[7], Keona Q. Wang[8], Nicolette R. Geller[9], Cristina Danita[1], Lydia-Marie Joubert[6], Michael F. Schmid[6], Serena Yeung[9], Judith Frydman[5], William Mobley[3], Chengbiao Wu[3], Leslie M. Thompson[2,7,8,10,11,+], Wah Chiu[1,6+]

Affiliations

[1]Department of Bioengineering, James H. Clark Center, Stanford University, Stanford, CA 94305, USA.

[2]Department of Psychiatry & Human Behavior University of California, Irvine, CA 92697, USA.

[3]Department of Neurosciences, University of California, San Diego, CA, USA.

[4]Department of Computer Science, Stanford University, Stanford, CA 94305, USA.

[5]Departments of Biology and Genetics, Stanford University, Stanford, CA 94305, USA.

[6]Division of CryoEM and Bioimaging, SSRL, SLAC National Accelerator Laboratory, Stanford University, Menlo Park, CA 94025, USA.

[7]Department of Memory Impairment and Neurological Disorders, University of California Irvine, Irvine, CA 92697, USA.

[8]Department of Neurobiology and Behavior, University of California Irvine, Irvine, CA 96267, USA.

[9]Departments of Biomedical Data Science, Computer Science and Electrical Engineering, Stanford University, Stanford, CA 94305, USA.

[10]Sue & Bill Gross Stem Cell Research Center, University of California Irvine, Irvine, CA 96267, USA.

[11]Department of Biological Chemistry, University of California Irvine, Irvine, CA 92617, USA.

* Co-first authors

+ Co-corresponding authors

To whom correspondence should be addressed:

Leslie M. Thompson; lmthomps@uci.edu; Wah Chiu; wahc@stanford.edu

29   **Abstract**

30   Huntington's Disease (HD) is caused by an expanded CAG repeat in the huntingtin gene, yielding

31   a Huntingtin protein with an expanded polyglutamine tract. Patient-derived induced pluripotent

32   stem cells (iPSCs) can help understand disease; however, defining pathological biomarkers is

33   challenging. Here, we used cryogenic electron tomography to visualize neurites in HD patient

34   iPSC-derived neurons with varying CAG repeats, and primary cortical neurons from BACHD,

35   deltaN17-BACHD, and wild-type mice. In HD models, we discovered mitochondria with enlarged

36   granules and distorted cristae, and thin sheet aggregates in double membrane-bound organelles.

37   We used artificial intelligence to quantify mitochondrial granules, and proteomics to show

38   differential protein content in HD mitochondria. Knockdown of Protein Inhibitor of Activated

39   STAT1 ameliorated aberrant phenotypes in iPSC-neurons and reduced phenotypes in BACHD

40   neurons. We show that integrated ultrastructural and proteomic approaches may uncover early

41   HD phenotypes to accelerate diagnostics and the development of targeted therapeutics for HD.

42   **Key Words:** Huntington's Disease, cryoET, iPSC, BACHD, mitochondria, aggregates, PIAS1

43   **INTRODUCTION**

44   Huntington's disease (HD) is a progressive, fatal neurodegenerative disorder caused by a genetic

45   mutation in the huntingtin gene (*HTT*)[1]. The mutation is an expansion of an N-terminal CAG

46   repeat to 40 and above. This yields a mutated Huntingtin protein (mHTT) with an expanded

47   polyglutamine (polyQ) tract that is pathogenic. Disease typically strikes in mid-life, lasting ~10-15

48   years with ongoing progression of symptoms, which include cognitive decline, mood and

49   personality disorders, and loss of motor control[2]. CAG length is correlated inversely with age of

50   disease onset with repeats longer than ~60 causing a juvenile form of HD[3,4]. No disease-modifying

51   treatments are available. Neuropathologically, degeneration of medium spiny neurons in the

52   striatum and cortical atrophy serve as prominent manifestations[5].

53   Methods to decipher the pathogenesis of neurodegenerative disorders are needed to identify

54   biomarkers sensitive to clinical progression and to inform therapeutic trials. A potential source

55   of such insights are patient-derived induced pluripotent stem cells (iPSCs)[6,7], which can be

2

56 differentiated into multiple cell types, including neurons[8] exhibiting disease phenotypes. Indeed,

57 a number of HD-associated phenotypes have been recapitulated in neurons differentiated from

58 HD iPSCs, including transcriptional dysregulation[4,9–12], bioenergetic deficits[13], impaired

59 neurodevelopment[9,14,15], altered cell adhesion[10,12], impaired nucleocytoplasmic trafficking[16,17]

60 and increased susceptibility to cell stressors[18], among others[18].

61 The propensity of mHTT to aggregate in neuronal cells is a hallmark of HD and leads to the

62 appearance of large (micrometer scale) nuclear and neuritic inclusions[19], as seen in mouse

63 models[20] and human[21] post-mortem brains[19,22]. Mutant HTT's role in the potential impairment of

64 autophagy may contribute to aberrant protein accumulation[23]. However, neither protein

65 aggregation nor disruptions to protein homeostasis have been observed in iPSC-derived HD

66 models unless treated with an inhibitor of the proteasome[24], likely because these models

67 represent early developmental stages where overt disease phenotypes are challenging to detect.

68 In parallel, other technological advances in cell, molecular and structural biology are poised to

69 contribute to the goal of identifying early pathology biomarkers. For example, advances in

70 cryogenic electron microscopy (cryoEM) and tomography (cryoET) have recently elucidated the

71 structure of soluble HTT in complex with HAP40 at near atomic resolution[25], the topology of

72 mHTT-exon 1 and polyQ *in vitro* aggregates at nanometer resolution[26], and have enabled

73 visualization of the interactions between mHTT-exon 1 aggregates and other proteins and cellular

74 compartments in transfected yeast[27] and HeLa[28] cells, and with molecular chaperones *in*

75 *vitro*[29,30]. Correlative light and traditional EM microscopy has also been used to image

76 recruitment of mHTT-exon 1 to cytoplasmic aggregates within single membrane, vesicle-rich

77 endolysosomal organelles[31].

78 Herein, we used cryoET to visualize neurites from five human iPSC-derived neuronal cell lines

79 endogenously expressing full-length mHTT with a range of CAG repeat lengths (Q18, Q53, Q66,

80 Q77 and Q109). Using the same methods, we also studied mouse primary neurons from the

81 BACHD model[32] expressing full-length human mHTT, full-length human mHTT lacking the first 17

82 amino acids (deltaN17; dN17)[33], and control WT mice. For all our samples, we examined

83 subcellular organelles previously implicated in HD, namely mitochondria[34] and

84   autophagosomes[35], and found marked changes in morphology as compared to controls. We then

85   coupled these ultrastructural observations with mitochondrial proteomics and found changes in

86   the levels of a number of mitochondrial proteins in HD samples. We also developed an artificial

87   intelligence-based semi-automated 3D segmentation method to quantify changes in

88   mitochondrial granule numbers and sizes.

89   Guided by combined ultrastructural and proteomic data, we explored the impact of genetic

90   knockdown (KD) of a SUMO E3 ligase Protein Inhibitor of Activated STAT1 (PIAS1), a protein linked

91   to maintenance of proteostasis and synaptic function in HD. In both systems, we observed rescue

92   of mitochondrial morphology. Additionally, PIAS1 reduction abrogated aberrant aggregates in

93   human HD iPSC-derived neuron autophagic organelles, findings consistent with prior studies

94   showing that PIAS1 inhibition ameliorates HD pathology in mice and human iPSCs[36].

95   Our investigations provide a platform with which to structurally evaluate *in situ* organelle

96   phenotypes in thin regions of intact cells at nanometer resolution, in the presence and absence

97   of potential therapeutics. The paradigm we propose emphasizes the ability to explore early

98   disease manifestations and mechanisms in neurites of intact patient and mouse model-derived

99   neurons, which serves as a proof of concept for the utility of cryoET as a structural readout to

100 assess early HD phenotypes and to support preclinical evaluation of potential therapies.

101 **RESULTS**

102 **Huntington's disease patient-derived iPSCs differentiated into mature neurons on electron**

103 **microscopy grids**

104 Neurons differentiated from human iPSCs with pathological- and normal-length polyQ tracts in

105 their *HTT* gene provide a platform to study different HD pathological states within their

106 endogenous genetic context[4]. Here, we developed a robust protocol to differentiate iPSC-derived

107 neurons with characteristics of medium spiny neurons on electron microscopy (EM) gold grids

108 (**Supplementary Fig. 1**).

109   We first differentiated iPSCs to neural progenitors and then adapted our prior maturation

110   protocol[4] to allow the cells to grow directly on gold EM grids, eliminating the Matrigel matrix to

111   minimize background densities, thereby maximizing contrast in cryoET images (**Supplementary**

112   **Fig. 1a)**. The cells survived, differentiated and matured without Matrigel, producing axons and

113   dendrites, and displaying normal neuronal morphology (**Supplementary Fig. 1b,c**).

114   Differentiation of cells was also performed at half density (see Methods) to increase the

115   likelihood of obtaining grids with only one cell per grid square, minimizing the potential for

116   overlaps between cells while maximizing the number of areas suitable for cryoET imaging

117   (**Supplementary Fig. 1c**). These modifications allowed iPSCs to differentiate into cells with

118   medium spiny neuron-like characteristics, as validated by DARPP32 and CTIP2 co-staining[12]

119   (**Supplementary Fig. 1d**). Cells were differentiated for 16 days, then plated on gold EM grids for

120   terminal differentiation and maturation. After three more weeks (21 ± 2 days) of terminal

121   differentiation, grids were vitrified by rapid plunging into liquid propane on day ~37-39[37,38] to

122   preserve the neurons on them in a near-native state without chemical fixative or metal stain.

123   **CryoET data showed mitochondria with abnormal cristae and enlarged granules in neurites of**

124   **HD patient iPSC-derived neurons**

125   The initial motivation to image intact human HD neurons using cryoET was to determine whether

126   we could directly visualize at nanometer scale *in situ* aggregates of native mHTT (endogenous

127   and untagged) that are not visible using other microscopy methods, as well as their surrounding

128   subcellular components. A single iPSC-derived neuron is a micrometer-sized cell with a thick cell

129   body and long, thin neurites. Since the electron beam cannot penetrate through the cell body of

130   neurons, we extensively surveyed the structural features in the neurites of our HD cells by

131   recording 2D cryoEM low-magnification projection images, from which we were able to identify

132   potential regions of interest for subsequent higher magnification cryoET data collection

133   (**Supplementary Fig. 2**).
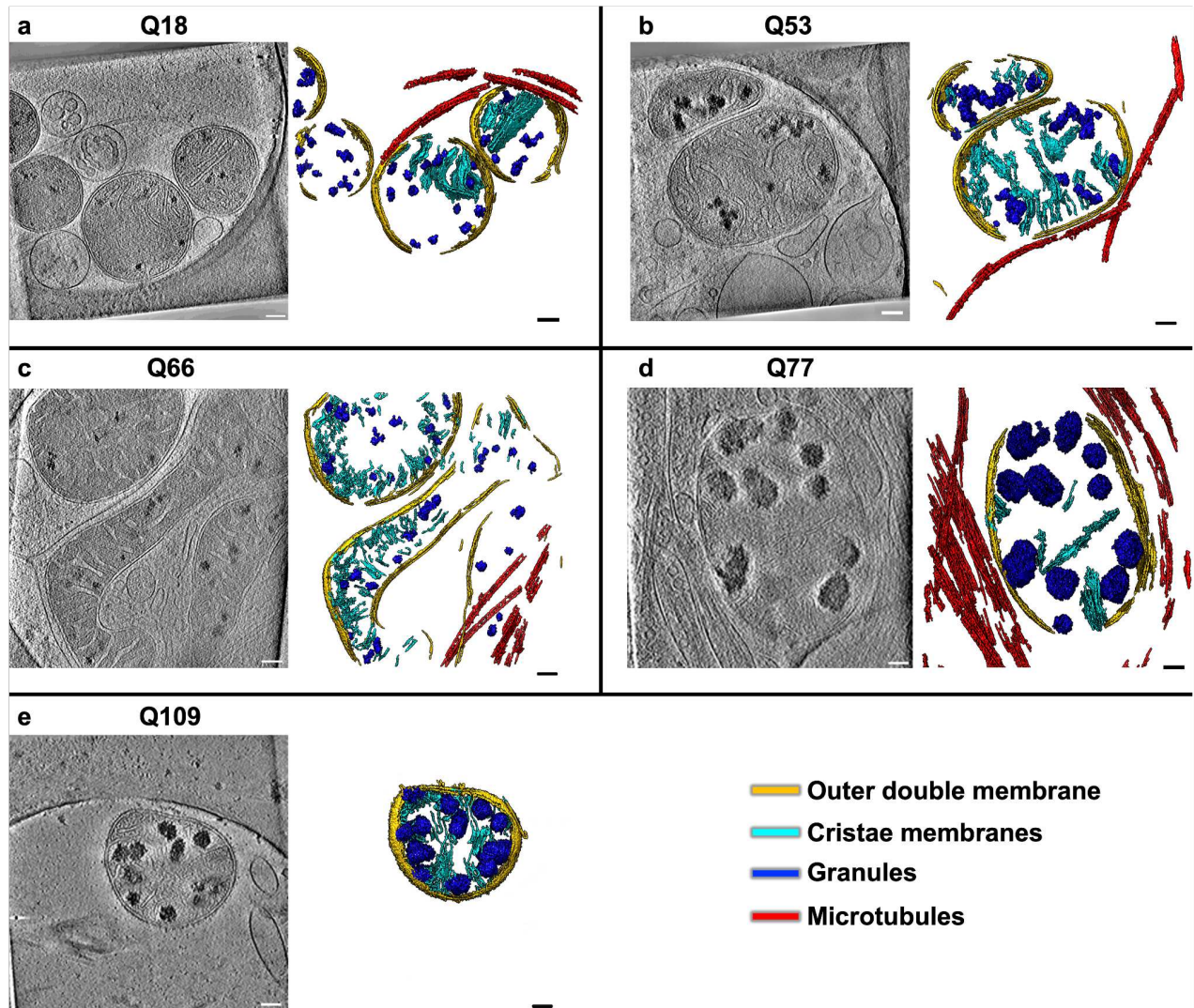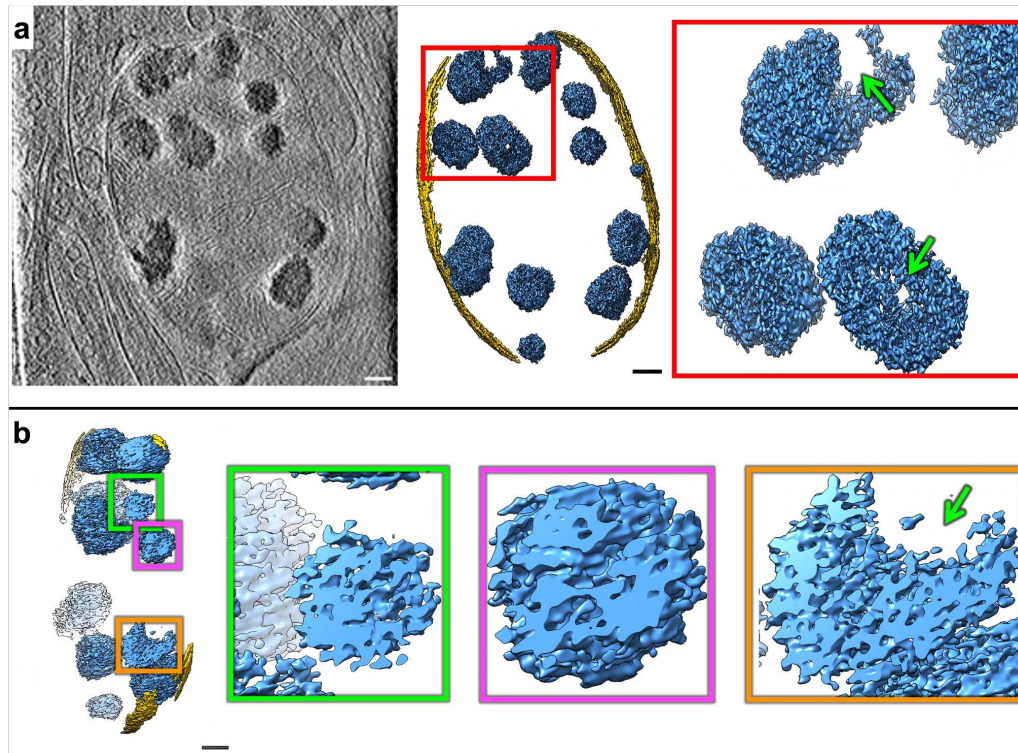
Fig. 1. Mitochondria in neurites of HD patient iPSC-derived neurons exhibit altered morphology and contain enriched granules of varying size. Slices (~1.4 nm thick) through selected regions of representative cryoET tomograms and corresponding segmentations of local features for **a** Q18, **b** Q53, **c** Q66, **d** Q77 and **e** Q109 human iPSC-derived neurons. Q53-Q109 reveal that mitochondria in HD patient-derived neurons have swollen cristae and contain enlarged granules compared to controls (Q18). Tomogram numbers: Q18=21, Q53=14, Q66=10, Q77=5 and Q109=37. Segmentation colors: red:microtubules, yellow:mitochondrial outer double-membranes, dark blue:granules, and cyan:cristae membranes. Scale bars = 100 nm.

Following an iterative search in many different areas on the cryoEM grids for all HD patient iPSC-derived (Q53, Q66, Q77 and Q109) neurons, we failed to detect large cytoplasmic inclusions or

146 aggregates such as those formed by mHTT-exon 1 previously observed by cryoEM/cryoET *in*

147 *vitro*[26,29,30,39,40] and in transfected cells[28,41]. However, this exhaustive examination did detect in

148 numerous regions in the neurites of all samples abnormally large and dense, discrete, granular

149 features as well as tangled aggregates, both within double membrane-bound compartments.

150 Some of these compartments showed classic features of mitochondria (**Fig. 1**), as marked by an

151 outer double membrane and the appearance of interior folded cristae, continuous with the inner

152 membrane of the compartment (**Supplementary Video 1**).

153 The large and dense granular features inside mitochondria were consistently present in tens of

154 tomograms of all HD cell lines (Q53, Q66, Q77 and Q109), and cristae were abnormal in most

155 mitochondria in higher polyQ lines (Q66, Q77 and Q109)(**Fig. 1c-e**). In general, both phenotypes

156 (namely, enlarged granules and disrupted cristae) became more pronounced with higher polyQ

157 length. Importantly, these aberrant features were absent from mitochondria of control iPSC-

158 derived neurons (Q18), though smaller features, consistent with normal mitochondrial granules,

159 were readily observed (**Fig. 1a**). To facilitate 3D visualization, we used the convolutional neural

160 network-based algorithm in EMAN2[42] to annotate and segment these dense structures as well as

161 other mitochondrial and subcellular features in surrounding areas, such as microtubules (**Fig. 1a-**

162 **e, Supplementary video 1**). Of note, the enlarged granules in mitochondria of HD cells did not

163 comprise homogeneous, smooth densities, but rather exhibited complex interwoven textures,

164 occasionally displaying lower-density regions or voids (**Fig. 2**).

165

Fig. 2. Mitochondria in HD neurites contain enlarged granules composed of tightly packed, heterogeneous densities. a Z-slice (~1.4 nm thick) through a representative cryoET tomogram of a neurite in an HD patient iPSC-derived neuron (Q77) and corresponding segmentation of double membranes (yellow) and dense, granular densities inside (light blue). **b** Cutaway, oblique view of the segmentation in **a** and zoomed-in views of selected regions showing examples of interwoven densities in enlarged mitochondrial granules. Green arrows point to void regions. Scale bars = 100 nm. Segmentation colors: yellow:double membrane, light blue:mitochondrial granules.

173

CryoET data showed mitochondria with abnormal cristae and enlarged granules in neurites of HD mouse model primary neurons

Next, we tested whether the abnormal ultrastructural features we observed in iPSC-neurons were also present in neurons derived from the well-studied BACHD mouse model[32], which expresses full-length human mHTT with an expanded polyQ tract comprised of 97 mixed CAG-CAA repeats under the control of human regulatory sequences. We used cryoET to image neurites in primary cortical BACHD neurons and again found abnormally enlarged granules within mitochondria whose cristae were often disrupted compared to WT (**Fig. 3a,b**), similar to those seen in neurites of HD patient iPSC-derived neurons (**Fig. 1b-e**). Our data are evidence that neurons from both human and mouse HD models share the presence of enlarged granules and other changes in mitochondria, supporting the view that mHTT is responsible and raising the

8

185   possibility that these morphological abnormalities could be used as diagnostic features. We also
186   evaluated primary cortical neurons from BACHD transgenic mice expressing human mHTT lacking
187   the first 17 N-terminal amino acids (dN17-BACHD)[33]. The N-terminus of HTT contains a putative
188   mitochondrial membrane-targeting sequence that can form an amphipathic helix[43,44]
189   characteristic of proteins transported into the mitochondria. This domain also promotes cytosolic
190   localization of HTT[45], potentially as a nuclear export sequence[46] and is required for interaction
191   with the subunit translocase of mitochondrial inner membrane 23 (Tim23), a mitochondrial
192   protein import complex essential for protein import[47]. Phenotypes are more robust and progress
193   more rapidly for dN17-BACHD than for BACHD mice[33], with nuclear and endoplasmic reticulum
194   (ER) mHTT localization for the former, as well as large nuclear inclusions visible by
195   immunofluorescence, which are not observed in the BACHD model[33]. CryoET of neurites in dN17-
196   BACHD neurons also showed severe distortions in most of their mitochondria (**Fig. 3c**). These
197   observations therefore suggest that mHTT can disrupt mitochondria via polyglutamine repeat-
198   dependent effects, such as those previously reported (using other techniques) to disrupt
199   mitochondrial membranes[48], independent of the N17 domain.

200
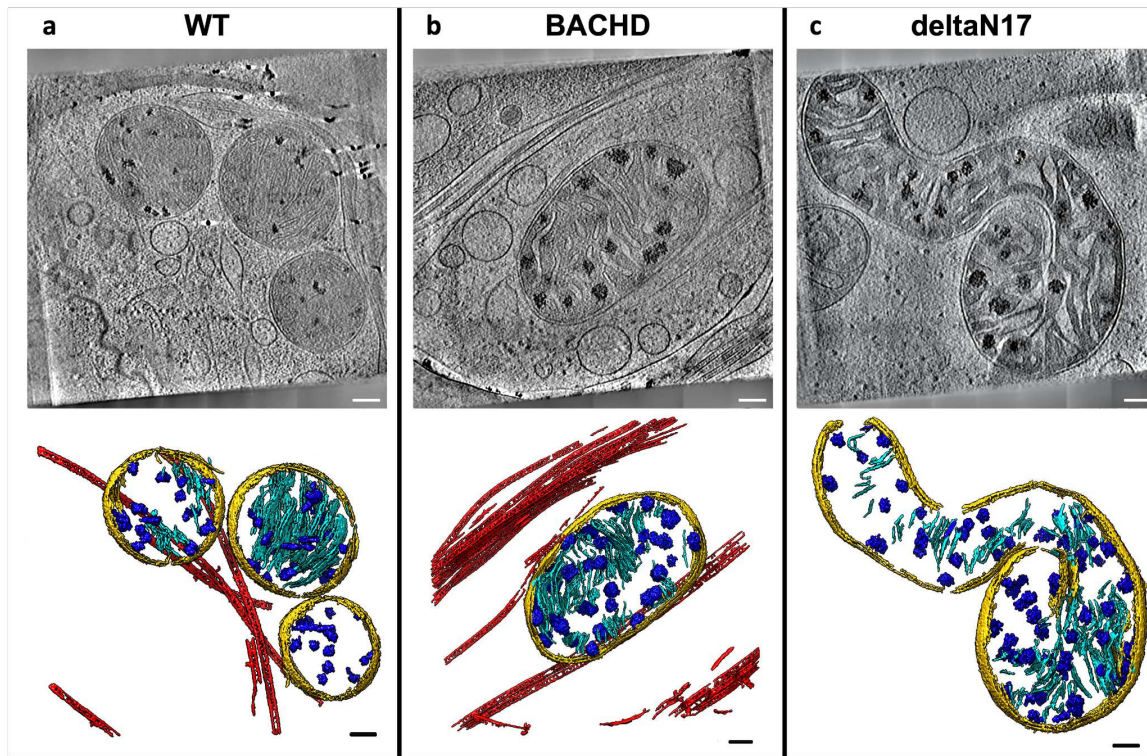
Fig. 3. Mitochondria in neurites of HD mouse model neurons exhibit altered morphology and contain
enlarged granules of varying size. Slices (~1.4 nm thick) through selected regions of representative cryoET
tomograms and corresponding segmentations of local features for **a** WT, **b** BACHD and **c** dN17 BACHD
primary neurons reveal that neuronal mitochondria in HD mice have swollen cristae and contain enlarged
granules compared to controls (WT). Tomogram numbers: WT=31, BACHD=22 and deltaN17 BACHD=15.

9

206 Segmentation colors: red:microtubules, yellow:mitochondrial double-membranes, dark blue:granules,
207 and cyan:cristae. Scale bars = 100 nm.

208

209 Neurites in HD patient iPSC-derived and mouse model neurons contain sheet-like aggregates

210 in autophagic organelles

211 In addition to the dense, enlarged granules observed in mitochondria, we observed numerous,
212 much larger aggregates in other membrane-bound compartments in both HD patient iPSC-
213 derived and mouse primary neurons. While they appeared to be filamentous when viewed in
214 two-dimensional (2D) z-slices through the tomograms, closer three-dimensional (3D) inspection,
215 including the use of UCSF ChimeraX's virtual reality (VR) graphics[49], revealed that they are
216 composed of densely interwoven slab-shaped, and sheet-like aggregates (**Fig. 4**, **Supplementary**
217 **Video 2**). Indeed, these aggregates had a distinct sheet morphology, similar to that of intricate
218 desert rose-like crystal of selenite, gypsum or barite found in the desert (hereafter called sheet
219 aggregates) [https://en.wikipedia.org/wiki/Desert_rose_(crystal)].

220 Importantly, these sheet aggregates were present in the neurites of all HD patient Qn neurons
221 (**Fig. 5a**)(Q53, Q66, Q77 and Q109) as well as in those of HD mouse model neurons (**Fig.**
222 **5b**)(BACHD and deltaN17 BACHD). On the other hand, double-membrane bound compartments
223 in neurites of control human iPSC-derived (Q18) (**Fig. 5c**) and mouse (WT) (**Fig. 5d**) neurons lacked
224 these sheet aggregates.

225 Of note, the sheets in these aggregates were reminiscent of some regions in mHTT exon 1 and
226 polyQ-only aggregates *in vitro*, shown to contain long, relatively flat or slightly curved ribbon-
227 like[50] or sheet-like[26] morphologies as visualized by negative stain electron microscopy and
228 cryoET, respectively. Interestingly, their thickness appeared relatively uniform, ~2 nm, when
229 visualized in our 3D tomograms with contrast transfer function correction and without
230 downsampling or low-pass filtration. Importantly, we also collected higher-magnification cryoEM
231 images of neurite regions with sheet aggregates and analyzed their Fourier transforms but did
232 not detect any periodic arrangement in them.

233
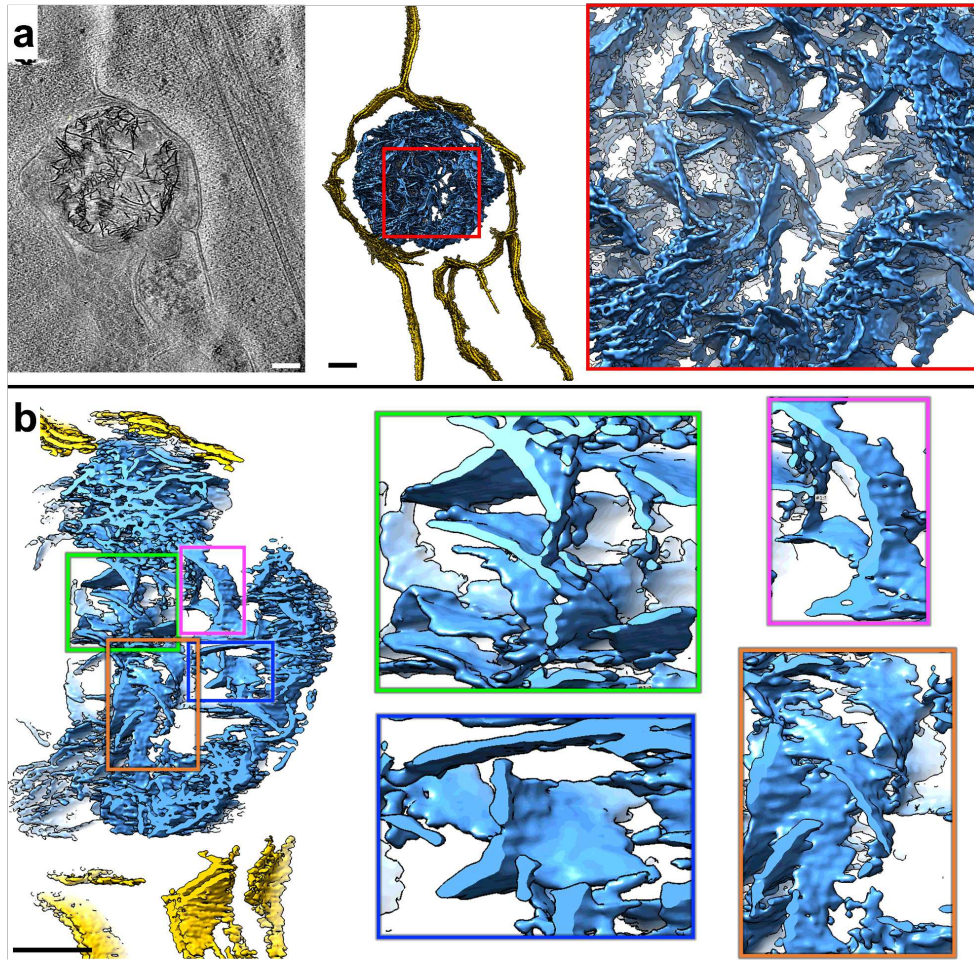
Fig. 4. Neurites in HD cells contain double membrane-bound compartments with sheet aggregates composed of interwoven slabs and sheets. a Z-slice (~1.4 nm thick) through a selected region showing a sheet aggregate in a representative cryoET tomogram of a neurite of a HD patient iPSC-derived neuron (Q66) and corresponding segmentation of double membranes (yellow) and aggregated densities inside (light blue). b Cutaway, oblique view of an enlarged region from the segmentation in a and further zoomed-in views of selected subregions showing examples of sheet-like areas within the aggregate. Scale bars = 100 nm. Segmentation colors: yellow:double membrane, light blue:sheet aggregate.

242
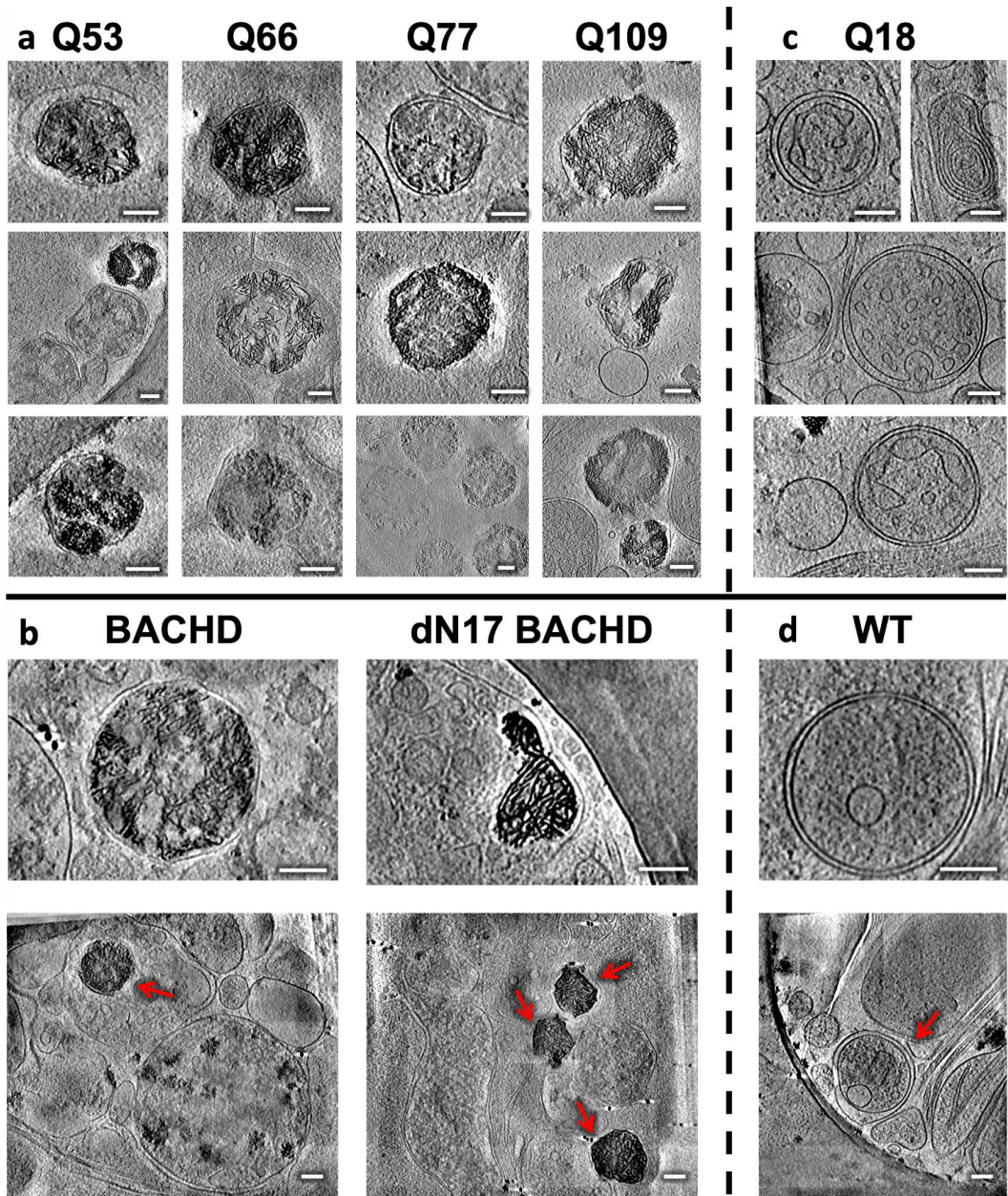
Fig 5. Neurites in HD patient iPSC-derived and mouse model primary neurons exhibit sheet aggregates within double membrane-bound organelles. Slices (~1.4 nm thick) through selected regions of representative cryoET tomograms showing double membrane-bound compartments in neurites of HD **a** patient iPSC-derived (Q53, n=5; Q66, n=8; Q77, n=6; Q109, n=6) and **b** mouse model (BACHD, n=14; and dN17-BACHD, n=6) primary neurons, as well as normal **c** Q18 (n=4) and **d** WT (n=3) controls. Scale bars = 100 nm. The red arrows in full-frame views in **b** indicate double membrane-bound organelles.

251 Eukaryotic cells contain several characteristic double membrane-bound compartments including

252 mitochondria, nucleus, and organelles in the autophagy pathway such as mitochondria-derived

253 vesicles[51], autophagosomes[52], and amphisomes[52]. Here, the compartments containing the sheet

254 aggregates (~200 nm to ~500 nm range in longest span) were much smaller than the nucleus (~3-

255 18 μm in diameter), and sometimes seemed to bind or merge with one another (**Supplementary**

256 **Fig. 3a**). While they were most often similar in size to small mitochondria, and could possibly

257 correspond to degenerating versions of this organelle or mitochondria-derived vesicles[51], there

258 is a possibility they may also correspond to other autophagic organelles with no visible cristae or

259 to other molecular components targeted for autophagy[52], suggesting alternative and possibly

260 complementary or parallel biogenesis origins. For instance, autophagosomes participate in

261 cellular pathways for degradation and clearance, and thus are possible candidates to contain

262 these sheet aggregates. Supporting this interpretation, we found instances of sheet aggregates

263 within double membrane-bound compartments fused with single membrane-bound

264 compartments (**Supplementary Fig. 3b-d**), reminiscent of lysosomes, a picture strikingly similar

265 to amphisomes, which result from fusion of autophagosomes with lysosomes[52]. On the other

266 hand, in support of the degenerating mitochondria assignment, we observed features suggestive

267 of nascent sheet aggregates in what appeared to be degenerating mitochondria (**Supplementary**

268 **Fig. 3e**). To further characterize the nature of these features, we again used semi-automated,

269 neural-networks-based annotation of the corresponding tomogram with EMAN2[42], training on a

270 few positive references (n=10) from a mature sheet aggregate only. Strikingly, the algorithm

271 assigned the putative nascent sheet aggregate features in what appears to be a mitochondrion

272 as belonging to the same type of feature as mature sheet aggregates, even though the networks

273 were trained exclusively with mature sheet aggregate references (**Supplementary Fig. 3f**). This

274 organelle could represent a degenerated mitochondrion bound with lysosomes, as these two

275 organelles were recently discovered to interact directly via their membranes[53]. Indeed, this

276 mitochondrion and a similar neighboring organelle are seen interacting with single membrane

277 bound compartments (**Supplementary Fig. 3g**).

278 **Mitochondrial proteomics of human iPSC-derived neurons identified differentially expressed**

279 **proteins, including those engaged in RNA binding**

280 The accumulation of mitochondrial granules (**Fig. 2**), distinctly different from the sheet

281 aggregates (**Fig. 4**), and the disruption of cristae observed in the neurites of HD neurons, are

282 consistent with impaired mitochondrial function and bioenergetics previously described for

283 HD[34,54]. This phenotype could represent aberrant accumulation of RNA granules[55], suggesting

284 RNA processing and RNA quality control deficits, and/or aberrant protein quality control due to

285 disrupted protein import arising from the presence of mHTT[47]. To investigate potential

286 mechanisms underlying the abnormal enlargement of mitochondrial granules, we performed

287 liquid chromatography tandem mass spectrometry-based proteomic analysis on mitochondria

288 isolated from HD patient iPSC-derived neurons (Q109) and controls (Q18) since the former

289 represents the most aggressive variant among our HD patient iPSC-derived samples (**Fig. 6**).

290 Mitochondria were isolated by using magnetically labeled anti-TOM22 microbeads[56]. Isolated HD

291 mitochondria looked similar in cryoEM projection images and reconstructed cryoET tomograms

292 (**Fig. 6a**) to those in neurites containing enlarged granules (**Fig. 1e**). In quality control

293 experiments, the mitochondrial isolation method was assessed via Western analysis on each cell

294 fraction; this yielded a fraction with enrichment of mitochondria (using ATPB protein levels as a

295 proxy) with some minor contamination from other organelles (LC3 levels were used as a proxy

296 for autophagosomes, and CTIP2 levels as a proxy for nuclei) (**Supplementary Fig. 4a**). Consistent

297 with successful isolation of mitochondria previously, our proteomic datasets were enriched for

298 Gene Ontology (GO) terms related to mitochondrial functions (**Supplementary Fig. 4b**).

299 Comparing the mitochondrial proteome of Q109 HD patient iPSC-derived neurons vs controls

300 (Q18) revealed a total of 177 differentially enriched peptides (DEPs), with a potential 236

301 identities, the majority of which were depleted in HD (**Fig 6b & Supplementary Table 3**).

302 Differentially enriched proteins included depletion of mitochondrial proteins (purple in **Fig. 6b**)

303 such as TOMM70A, a mitochondrial import receptor involved in the translocation of preproteins

304 into mitochondria, which is impaired in HD[48]. We also detected a depletion of ER proteins in HD

305 mitochondria (orange in **Fig. 6b**), which could reflect impaired mitochondria-ER interactions[57]

306 and well-documented ER dysfunction in HD[58,59]. Interestingly, FIS1 (mitochondrial fission protein)

307 levels were increased in HD (**Fig. 6b**), consistent with previous data showing altered regulation

308 of mitochondrial fission in HD[60,57].
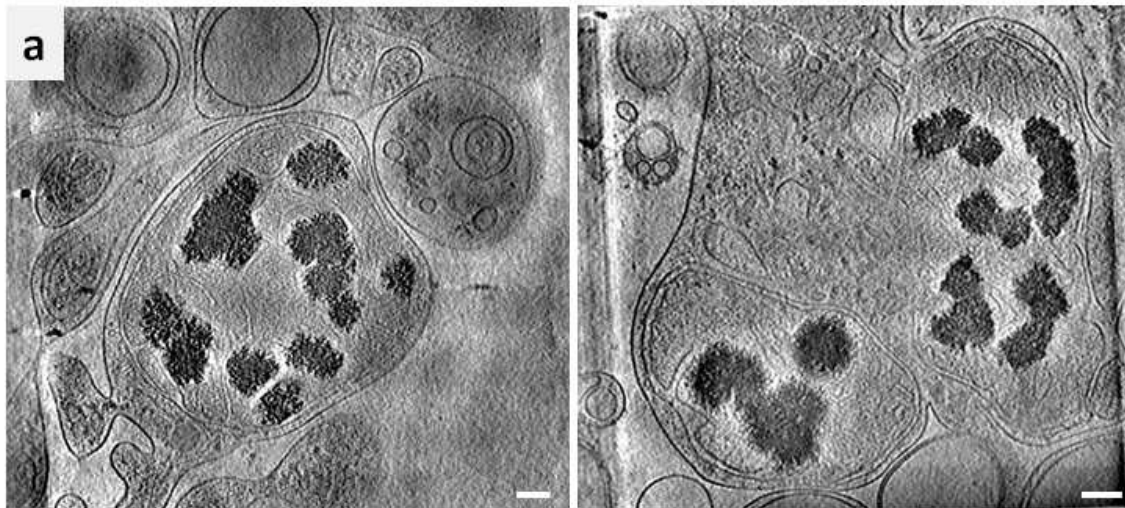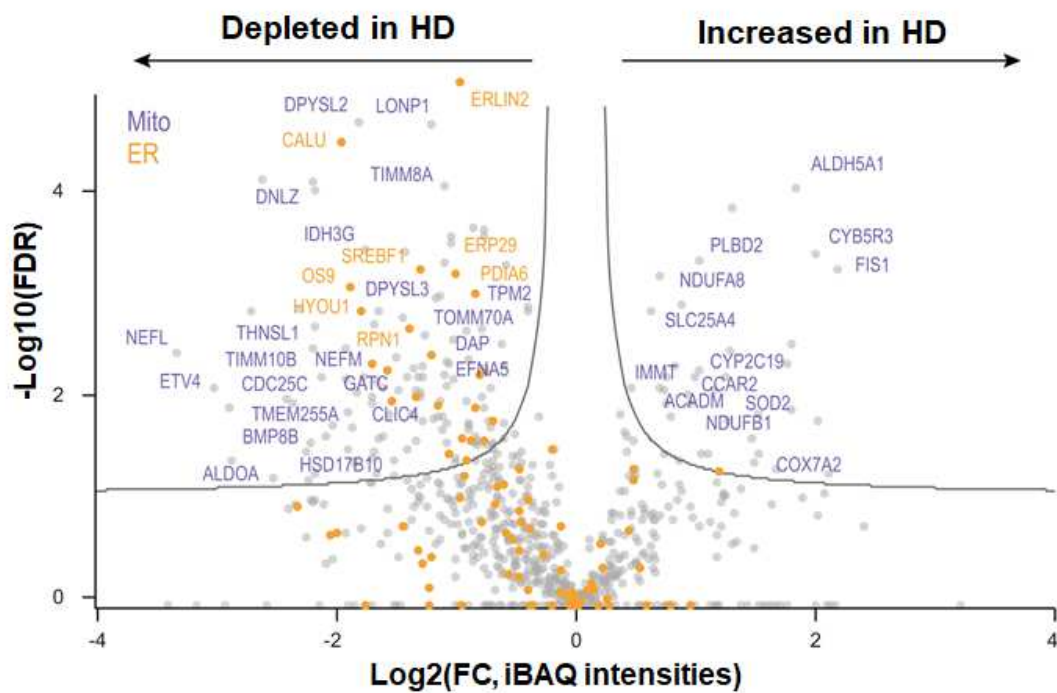
Fig. 6. Mass spectrometry of isolated mitochondria revealed differentially enriched proteins (DEPs) in neurites of HD patient iPSC-derived neurons (Q109) vs controls with cryoET showing accumulation of granules in such HD mitochondria. **a.** Z-slices (~1.4 nm thick) through representative cryoET tomograms of isolated Q109 mitochondria showed abnormal accumulation and enlargement of mitochondrial granules. Scale bars = 100 nm. **b** Mass spectrometry of proteins in isolated mitochondria showed 177 differentially enriched peptides with a potential of 236 protein identities. The scatter plot highlights
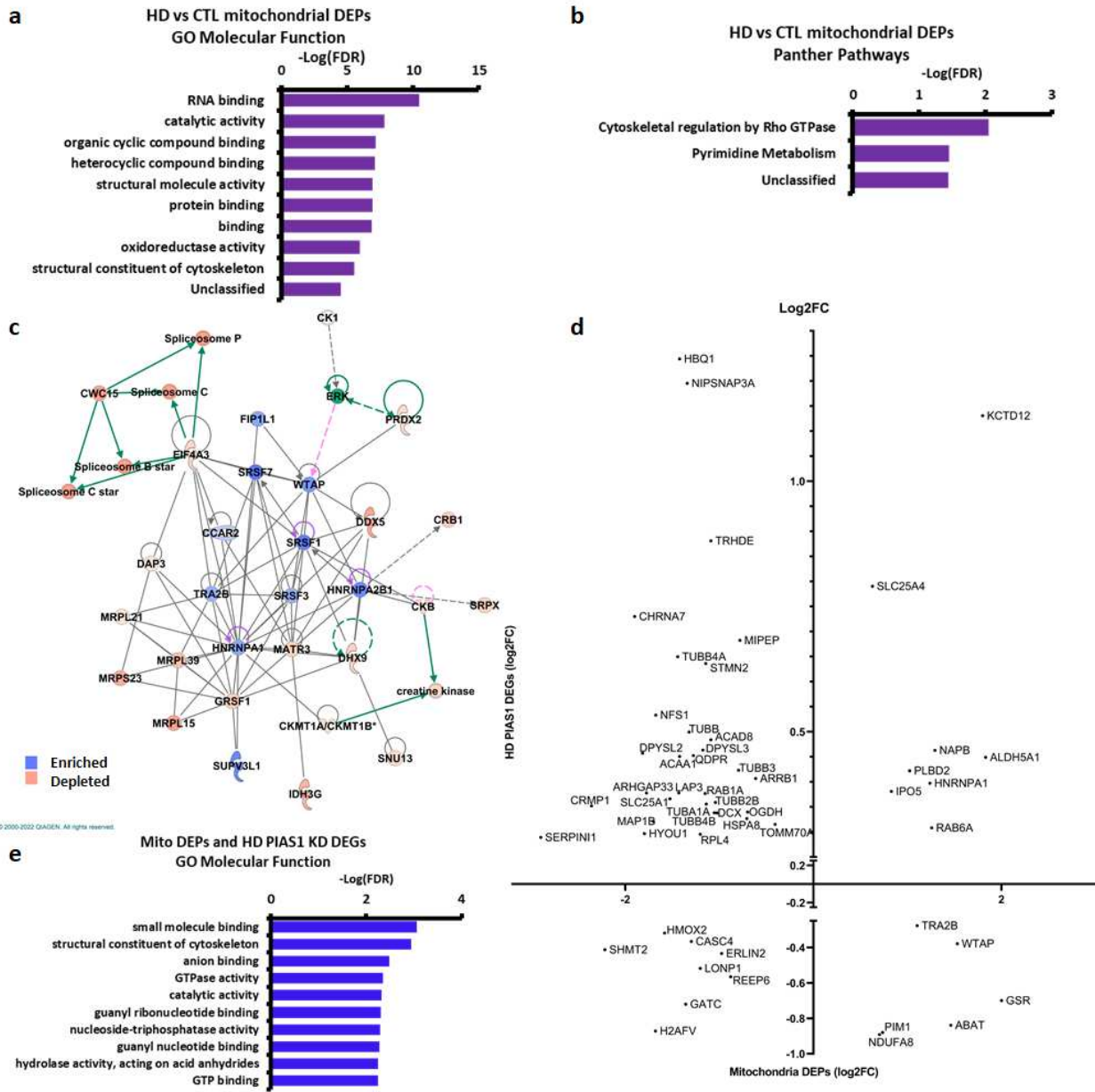
316 selected proteins that were depleted or increased in HD (Q109) mitochondria in comparison to controls

317 (Q18). Mitochondrial proteins are highlighted in purple and ER proteins in orange.

318

319 GO analysis of the differentially enriched peptides found RNA binding to be the most enriched

320 molecular function (**Fig. 7a**), as reflected by increased levels of various cytoplasmic RNA binding

321 proteins such as hnRNPA2B1, hnRNPA1 and hnRNPH1. On the other hand, GRSF1, a

322 mitochondrial RNA binding protein[61], showed reduced levels in HD mitochondria. This protein is

323 essential for mitochondrial function and required for mitochondrial RNA processing[62]. Indeed,

324 loss of GRSF1 causes mitochondrial stress and can induce senescence phenotypes[63]. Panther

325 pathway analysis identified cytoskeletal regulation by Rho GTPase and pyrimidine metabolism as

326 two other of the three most overrepresented pathways by the DEPs (**Fig. 7b**).

327 Ingenuity Pathway Analysis (IPA) of the mitochondrial DEPs identified a network representing

328 proteins involved in molecular transport, RNA post-transcriptional modification and RNA

329 trafficking, potentially further implicating these proteins in RNA biology and dynamics (**Fig. 7c**).

330 Upstream regulators identified by IPA included Amyloid Precursor Protein (APP) and

331 transforming growth factor β (TGF-β) as predicted inhibitors of the mitochondrial DEPs in HD. IPA

332 pathways included mitochondrial dysfunction, consistent with the mitochondrial deficits in HD[64]

333 (**Supplementary Fig. 5c-f**).

334

a HD vs CTL mitochondrial DEPs GO Molecular Function

b HD vs CTL mitochondrial DEPs Panther Pathways

c (network diagram with Enriched/Depleted legend)

d Log2FC scatter plot

e Mito DEPs and HD PIAS1 KD DEGs GO Molecular Function

335

Fig. 7. Analysis of mass spectrometry data from isolated HD (Q109) vs control mitochondria showed RNA binding and an overlap with PIAS1 knockdown differentially expressed genes (DEGs). a Graph of gene ontology (GO) analysis of the potential 236 identities of the DEPs in HD vs control mitochondria showing molecular functions overrepresented by HD DEPs. **b** Graph of Panther analysis of the 236 DEPs in HD vs control mitochondria showing Panther Pathways overrepresented by HD mitochondria DEPs. **c** Ingenuity pathway analysis of the differentially enriched proteins between HD and control mitochondria highlighted this as the top network (score, 55 Focus molecules: 28), and represents Molecular Transport, RNA Post-Transcriptional Modification, and RNA Trafficking. Proteins in orange are depleted in HD while proteins in blue are enriched. **d** Scatter plot of overlapping DEG log2 fold changes generated from PIAS1 knockdown in HD iPSC-derived neurons from previous work[65] plotted against the log2 fold enrichment of

17

346   mitochondrial DEPs. **e** GO analysis of molecular functions overrepresented by the 55 overlapping

347   DEPs/DEGs that are in **d**. N=3 per control and HD samples.

348

349   ***PIAS1* heterozygous knockout in HD patient iPSC-derived neurons and short-term *Pias1***

350   **knockdown in BACHD mouse neurons rescues aberrant mitochondrial granules and presence**

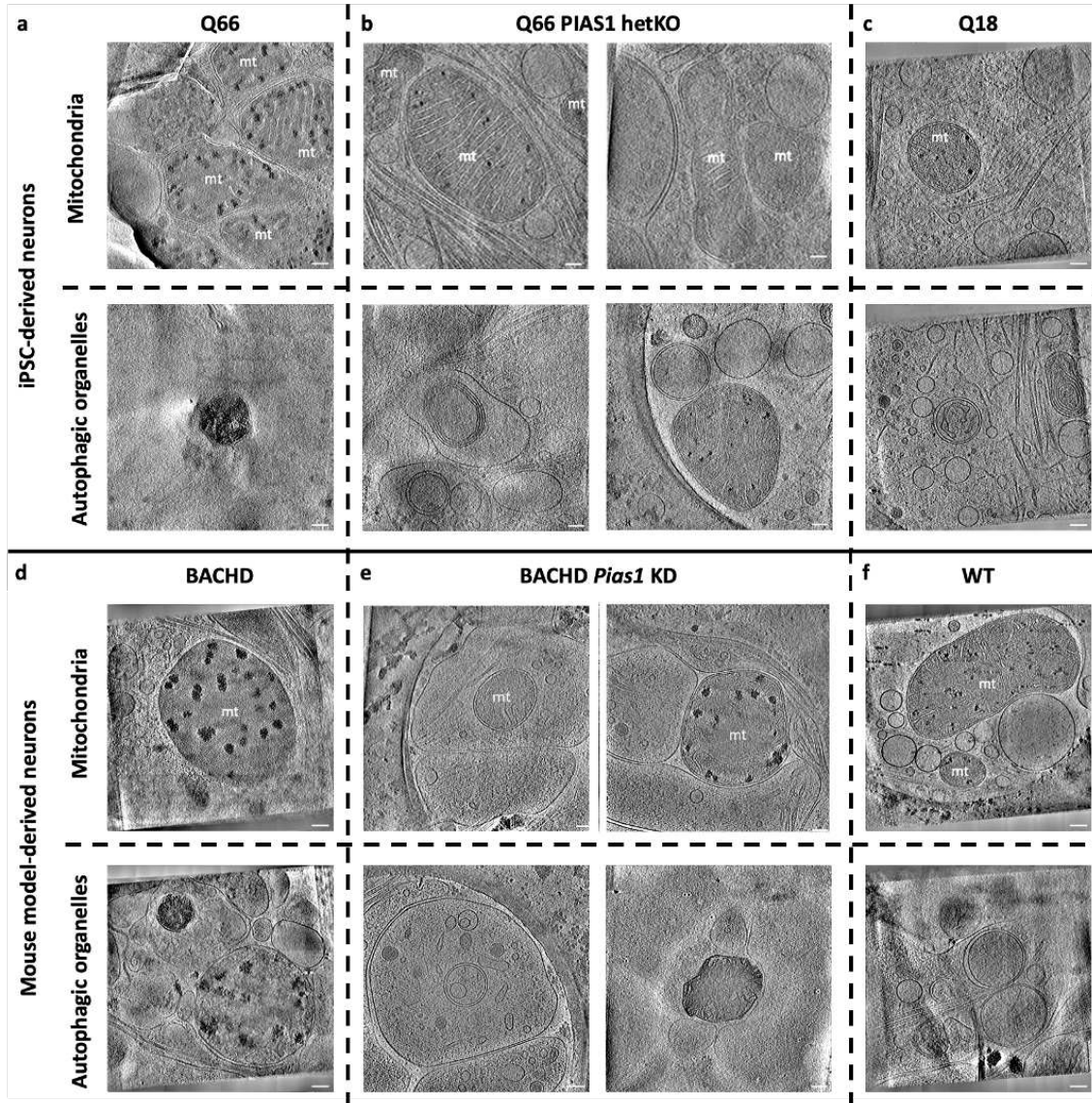351   **of sheet aggregates in neurites**

352   Mitochondrial dysfunction can be highly detrimental to neuronal function, particularly in light of

353   the extensive energetic requirements for synaptic function[66]. To evaluate whether the observed

354   phenotypes can be ameliorated, we evaluated genetic reduction of an E3 SUMO ligase, PIAS1,

355   based on our previous data showing that reduced *Pias1* expression resulted in: increased

356   expression of the presynaptic protein synaptophysin in R6/2 HD mice, rescued transcriptional

357   synaptic deficits in zQ175 HD mice, and improved mitochondrial DNA integrity and synaptic gene

358   expression in iPSC-derived neurons[65,36]. PIAS1 enhances SUMOylation of various proteins,

359   including HTT[45,67]. To computationally determine whether targeting PIAS1 would predict changes

360   in the HD mitochondrial proteome, we first compared the changes in the mitochondrial

361   proteome of HD iPSC-derived neurons (Q109 vs Q18) described above with findings from our

362   prior study of gene expression in the same type of differentiated neurons following PIAS1

363   knockdown[65] (**Fig. 7d**). We found a significant overlap between mitochondrial DEPs and RNA

364   changes induced by siRNA depletion of PIAS1 in HD iPSC-derived neurons (representation

365   factor:1.9 p<2.081e-06, **Fig. 7d, Supplementary Fig. 5a**, **Supplementary Table 3**). This overlap of

366   genes and proteins included overrepresentation of GO terms including "GTP binding" and

367   "GTPase activity" as well as several RNA processing-related proteins and tubulins[65] (**Fig. 7e**).

368   These comparisons further supported investigating whether knockdown of PIAS1 could influence

369   the presence and/or size of the aberrant granules we observed within HD mitochondria.

370   We again used cryoET to visualize iPSC-derived neurons (Q66, representing an intermediate

371   range of phenotypes) with *PIAS1* heterozygous knockout (hetKO), using a CRISPR-Cas9-generated

372   heterozygous KO, which produces approximately 50% knockdown (**Supplementary Fig. 5e,f**). The

373   *PIAS1* KD iPSC neurons (Q66) differentiated well on EM gold grids in preparation for cryoET

374   experiments (**Supplementary Fig. 5g**). The Q66 *PIAS1* hetKO tomograms (**Fig. 8**) showed

375   seemingly healthy mitochondria and other double membrane-bound organelles (**Fig. 8b**), lacking

376   the abnormally enlarged granules and sheet aggregates, respectively, as had been observed in

377   HD patient iPSC-derived neurons for all Qns (**Fig. 1, 5 & 8a**). Indeed, the structural features of

378   Q66 *PIAS1* hetKO neurites resembled those from control Q18 neurons (**Fig. 8c**) rather than Q66

379   ones.

380   To determine if the rescue of abnormal morphologies observed in HD patient iPSC-derived

381   neurons (Q66) treated with *PIAS1* KD translates to mouse cortical neurons, we carried out a

382   short-term *Pias1* KD in mouse primary neuronal cultures derived from E18 BACHD cortical

383   neurons on EM grids and visualized cells with cryoET (**Fig. 8**). To reduce *Pias1* levels, Accell

384   (Dharmacon) siRNA smart pools against mouse *Pias1* were used. *Pias1* KD was initiated at day *in*

385   *vitro* 3 (DIV3) with one treatment and grown for 11 days. Cells were vitrified for cryoET analysis

386   at DIV14. Knockdown of *Pias1* in the BACHD neurons was successful according to qRT-PCR

387   analyses*;* 43% knockdown was achieved comparing control-siRNA-treated neurons to *Pias1*

388   knockdown (**Supplementary Fig. 5i,j**).

389   CryoET experiments showed that treating BACHD neurons with *PIAS1* siRNA resulted in partial

390   rescue. Indeed, while many mitochondria completely lacked detectable granules, visibly reduced

391   in comparison to the BACHD mitochondria, sheet aggregates in autophagic organelles were

392   present in comparable numbers to those in BACHD neurons without *Pias1* KD (**Fig. 8e,** bottom

393   right). Thus, the beneficial effects of *PIAS1* hetKO in HD patient iPSC-derived neurons was only

394   partially replicated in the mouse model under our experimental conditions, possibly due to the

395   later and shorter treatment time frame. Whether the impact of PIAS1 reduction is consistent

396   across all cells or results in different effects in different cell types needs further investigation.

Fig. 8. Reduced *PIAS1* rescues mitochondrial granule size and sheet aggregates in neurites of HD model neurons. Slices (~1.4 nm thick) through representative cryoET tomograms of neurites in **a** Q66, **b** *PIAS1* hetKO, and **c** Q18 iPSC-derived neurons show that *PIAS1* hetKO ameliorated the phenotypes of enlarged mitochondrial granules (first row) and sheet aggregates in putative autophagic organelles (second row) in HD iPSC-derived neurons (Q66). Slices (~1.4 nm thick) through representative cryoET tomograms of neurites in **d** BACHD, **e** BACHD *Pias1* KD, and **f** WT mouse neurons show that *Pias1* KD ameliorated the enlarged mitochondrial granules (third row) but not the sheet aggregates in putative autophagic organelles (fourth row) in BACHD-derived neurons.

20

Artificial intelligence-based semi-automated 3D segmentation enabled quantification of abnormally enlarged mitochondrial granules in neurites from HD patient iPSC-derived neurons and mouse model primary neurons

We observed both enlarged granules and disrupted cristae in the mitochondria of HD neuronal processes (**Fig. 1-3**). The mitochondrial granules varied in size, seeming much larger in HD mitochondria than in controls. To quantify their size distribution, we developed a semi-supervised artificial intelligence method to automatically detect and segment mitochondria and mitochondrial granules in the neurite tomograms (**Supplementary Fig. 6**). Among all tomograms (**Supplementary Table 1**), the algorithm found that 139 contained mitochondria for the various HD patient iPSC-derived neurons and 83 for mouse model neurons (**Supplementary Table 1**).
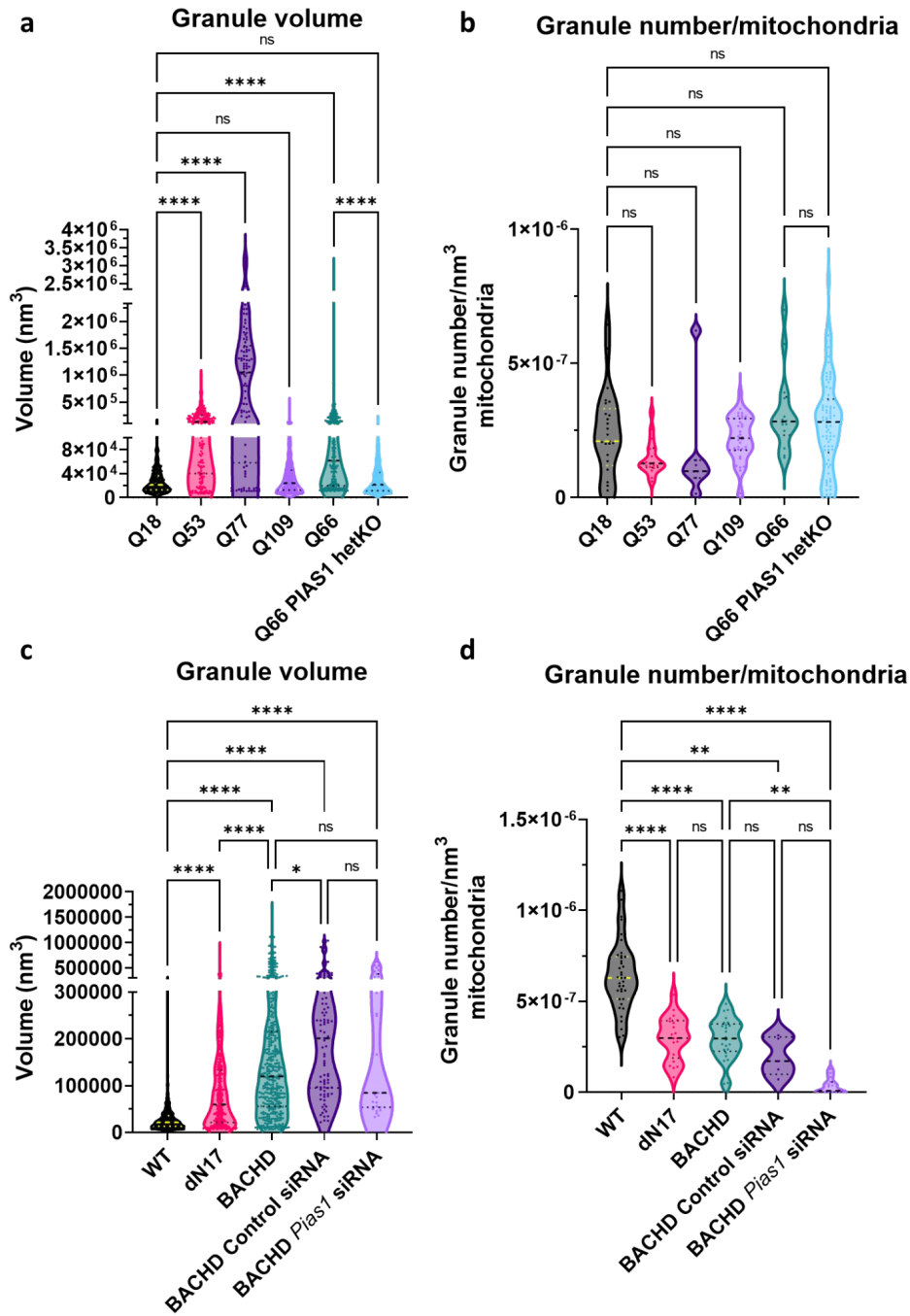
Using quantification of the granule volumes by segmentation estimation, our algorithm revealed that the distribution of mitochondrial granule volumes was shifted towards larger sizes with respect to controls for Q53, Q66, and Q77 (**Figure 9a**), as well as for BACHD, dN17-BACHD, BACHD *Pias1* siRNA, and BACHD transfected with a control siRNA (**Figure 9c**). On the other hand, granule volumes were not larger in Q109 compared to Q18 controls, and were significantly decreased in the Q66 PIAS1 hetKO line when compared to Q66 (Dunn's multiple comparison Q66 vs. Q66 PIAS1 hetKO padj<0.0001), resembling results for the control Q18 line.

Surprisingly, granule volumes were not statistically reduced in BACHD treated with *Pias1* siRNA in comparison to BACHD (Dunn's multiple comparisons BACHD vs. BACHD *Pias1* siRNA padj>0.9999). On the other hand, control siRNA-treated BACHD neurons showed no difference in granule size distribution compared to *Pias1* siRNA treatment, as expected, given that the latter had no effect (Dunn's multiple comparisons BACHD Control siRNA vs. BACHD Pias1 siRNA padj>0.9999). Lastly, there was an unexpected modest increase in granule volumes in BACHD upon control siRNA treatment.

While granule volumes were increased for all Qn iPSC-derived neurons except Q109, granule numbers per nm^3 of mitochondrial volume were not different in any of them from those in

433   control Q18 cells. On the other hand, granule numbers per nm³ of mitochondrial volume were

434   decreased in all mouse cell lines with respect to WT, including in those treated with siRNAs.

435

436

437   **Fig. 9**: **Artificial Intelligence (AI)-based 3D quantification of mitochondrial granule volume and granule**

438   **number per nm³ of mitochondrial volume in cryoET tomograms of mitochondria in neurites**

439 **demonstrates a significant increase in granule size with higher polyQ in HD human and mouse model**
440 **neurons and this is rescued in the Q66 PIAS1 hetKO neurons**. Violin plots displaying AI measurements of
441 mitochondrial granule **a** volume (Kruskal Wallis statistic = 401.3, P value<0.0001) and **b** numbers per nm^3
442 of mitochondrial volume (Kruskal Wallis statistic = 19.78 P= 0.0014) from cryoET tomograms of neurites
443 for five HD patient iPSC-derived neuronal cell lines (tomogram numbers: Q18=21, Q53=14, Q66=10,
444 Q77=5, Q109=37 and *PIAS1* hetKO=68; granule number:Q18=250, Q53=176, Q66=250, Q77=94,
445 Q109=539 and *PIAS1* hetKO=923) as well as mitochondrial granule **c** volume (Kruskal Wallis statistic =
446 750.8, P<0.0001) and **d** numbers per nm^3 of mitochondrial volume (Kruskal Wallis statistic = 77.48,
447 P<0.0001) from cryoET tomograms of neurites for three mouse neuron models (tomogram numbers:
448 WT=31, BACHD=22, dN17 BACHD=15, BACHD control siRNA=5 and BACHD *Pias1* siRNA=12; granule
449 numbers: WT=1338, BACHD=380, dN17-BACHD=326, BACHD control siRNA=91 and BACHD *Pias1*
450 siRNA=27). The human neurons and mouse model neurons showed an increase in granule volumes in all
451 but Q109, a trend of reduced granule number in human neurons and a significant reduction in granule
452 number in mouse model neurons. ns=not significant, **** p<0.0001, ** p<0.01, * p<0.05 For full statistical
453 details refer to **Supplementary Table 2**.

454

455 **DISCUSSION**

456 In this study, we have defined Q-length dependent ultrastructural changes that occur in neuronal

457 processes (neurites) of human HD iPSC-derived neurons and BACHD primary cortical neurons.

458 Specifically, we found that HD neurons contain two types of double membrane-bound organelles

459 with abnormal densities inside, which are completely absent in healthy control neurons. First, we

460 observed ultrastructural changes in neuronal mitochondria, most notably enlarged granules in

461 all HD samples compared to controls (**Fig. 1-3**). Importantly, many HD samples also exhibited

462 severely disrupted cristae, similar to cryoET observations in other neurodegenerative disorders

463 such as Leigh syndrome[68]. Second, we observed sheet aggregates within autophagic organelles

464 resembling mitochondria-derived vesicles, autophagosomes and/or amphisomes (**Fig. 4, 5,**

465 **Supplementary Fig. 3**). These findings are highly significant in demonstrating the disruption of

466 organellar structure in HD, possibly as very early events in pathogenesis that precede overt

467 neuronal dysfunction and the appearance of inclusions visible in neurons derived from HD

468 patient[21] and mouse model[20,69] brain tissues .

469 Cellular cryoET experiments ultimately yield 3D volumes ("tomograms") that sample regions of

470 the crowded subcellular environment in intact cells. Generally, an experienced investigator

471 would use visualization graphics to inspect one tomogram at a time, a laborious discovery process

472 requiring expert knowledge. In the initial stages of this project, we visualized hundreds of neurite

473 tomograms, leading to the discovery of enlarged granules in mitochondria and sheet aggregates

474 in autophagic organelles within them. Using a newly developed semi-supervised artificial

475 intelligence-based method to segment and quantify the number and volume of mitochondrial

476 granules (**Supplementary Fig. 6**), we found that their enlargement is a structural signature of HD,

477 consistently present in both human iPSC- and mouse model-derived neurons (**Fig. 9**).

478 The aberrant accumulation of large mitochondrial granules and abnormal cristae are known

479 hallmarks of mitochondrial dysfunction as assayed by other methods in similar systems[34,54]. As

480 members of the HD iPSC Consortium[10], we previously showed using cell biology techniques that

481 striatal-like HD iPSC-neurons similar to those examined here have mitochondrial deficits

482 including altered mitochondrial oxidative phosphorylation. Indeed, we demonstrated impaired

483 oxygen consumption rate (OCR), altered spare glycolysis capacity (ECAR) and reduced ATP levels

484 in HD neurons[13]. Additional studies have also shown mitochondrial dysfunction, fragmentation

485 and disrupted cristae by traditional electron microscopy of chemically fixed cell lines expressing

486 mHTT[70].

487 The high scattering contrast of the enlarged granules we observed here in both human and

488 mouse HD model neurons could be attributable to RNA and/or calcium phosphate, which are

489 more electron dense and thus scatter the electron beam more strongly than most other

490 molecular components in mitochondria comprised of lighter elements such as carbon, nitrogen

491 and oxygen. Our mass spectroscopy data (**Figs. 6, 7 & Supplementary Fig. 4**) are consistent with

492 either interpretation. Indeed, assessing the proteome of mitochondria isolated from human HD

493 iPSC-derived neurons identified differentially enriched proteins related to protein import and

494 RNA binding (**Fig. 7**). RNA granules are normal features of the mitochondrial matrix[61], and are

495 composed of newly synthesized RNA, RNA processing proteins and mitoribosome assembly

496 factors[61,71–73]. Stressors such as dysregulation of RNA processing and RNA quality control defects

497 can cause aberrant accumulation of mitochondrial RNA granules, which comprise large

498 ribonucleoprotein complexes[55]. RNA granules are components of mitochondrial post-

499   transcriptional pathways and are responsible for mitochondrial RNA translation[74]. When these

500   granules aberrantly accumulate, the integrity of cristae is compromised to accommodate them[71].

501   GRSF1, a nuclear encoded RNA-binding protein that regulates RNA processing in mitochondrial

502   RNA granules[62] and is critical for maintaining mitochondrial function[63,75], was significantly

503   decreased in our mitochondrial proteomic dataset in HD. GRSF1 has also been implicated in

504   cellular senescence with levels declining in senescent cells and lowered GRSF1 levels causing

505   mitochondrial stress[63]. Further evidence that these structures may represent mitochondrial RNA

506   granules is the enrichment of RNA binding proteins in the proteome of HD iPSC-derived neurons

507   versus controls.

508   Alternatively, mitochondria are known to normally contain calcium phosphate granules, which

509   store excess calcium, maintain mitochondrial calcium concentration, and contribute to

510   maintenance of mitochondrial function[76,77]. Furthermore, calcium overload within cells is known

511   to cause ultrastructural remodeling of cristae[63,78], as in our experimental results described above,

512   which was particularly profound for Q109 neurons and dN17-BACHD neurons. Cellular calcium

513   dyshomeostasis is a well-established phenotype in HD[79,80], wherein an increase in store-operated

514   calcium entry (SOCE) can lead to increased calcium uptake by the mitochondria due to their

515   proximity to the ER[80], ultimately resulting in increased mitochondrial granule size due to

516   increased calcium uptake. Furthermore, mitochondrial calcium dysregulation was observed in

517   mitochondria isolated from transgenic YAC128 HD mice[81]. HD mitochondria are more susceptible

518   to calcium stress and form megapores more readily than control mitochondria[82]. Sequestration

519   of calcium into the mitochondria can protect neurons from glutamate excitotoxicity, a phenotype

520   observed in HD neurons[83,84]. Thus, the enlarged mitochondrial granules we observed here across

521   multiple human and mouse HD model neurons may be composed at least in part of excess

522   calcium phosphate.

523   The two most likely possibilities for the chemical identity of enlarged mitochondrial granules (*i.e.*,

524   RNA granules versus calcium phosphate granules) need not be mutually exclusive. While future

525   studies such as elemental analysis with electron and/or x-ray microscopy[85] could help define the

526   chemical nature of these granules, our data provide clues as to their genesis and development.

527 In iPSCs, granule volume is significantly increased in all cell lines examined herein, except Q109

528 (**Fig. 9a**), whereas the number of granules per nm^3 of mitochondrial volume in all iPSC cell lines

529 is not significantly different from that in controls (**Fig. 9b**). This suggests that as new granules or

530 the materials that form them become available, they coalesce with each other and/or with

531 existing ones. On the contrary, for mitochondria in BACHD mice, the larger size of the granules

532 (**Fig. 9c**) is accompanied by a significant reduction in their number (**Fig. 9d**) with respect to

533 controls, suggesting that smaller granules may grow primarily by aggregation with other existing

534 granules rather than by addition of new materials. Further experiments are needed to elucidate

535 the chemical compositions of these granules, which will in turn allow probing for the production

536 of their component materials during neurodegeneration.

537 Interestingly, granule volumes are larger in iPSC Q66 and Q77 than in our HD mouse models,

538 despite BACHD containing mHTT with a longer polyQ tract (Q97). This may be attributable to

539 differences in the biology of the model systems. Another possible explanation for the statistical

540 discrepancy between cell lines and model systems is that Q53 through Q77 might predictably be

541 in a different (earlier) stage of neurodegeneration than Q109, the latter perhaps being in a state

542 more comparable to BACHD neurons. Importantly, recapitulation in multiple human iPSC lines of

543 the same structural phenotypes seen in mouse primary neurons helps to validate iPSCs as useful

544 HD models.

545 We also observed differences in the mitochondrial phenotype between the mouse models. While

546 both BACHD and dN17-BACHD mice showed enlarged mitochondrial granules with respect to

547 controls (albeit fewer in number), dN17-BACHD displayed smaller granules than BACHD and

548 severely distorted structures, such as seemingly enlarged mitochondria and swollen cristae. The

549 difference in granule size between BACHD neurons and those treated with control siRNA may be

550 attributable to off-target effects of the control siRNA, timing of treatment or Accell delivery in

551 general. Nonetheless, taken together, our data provide additional hints regarding potential

552 mechanistic underpinnings of normal HTT function. In HD, mitochondrial function appears to be

553 impacted by the altered import of mitochondrial precursor proteins in the presence of mutant

554 HTT[47]. Indeed, the high affinity interaction of mHTT with the inner mitochondrial protein import

555 complex subunit TIM23 disrupts the HD mitochondrial proteome[48]. Furthermore, protein

556 aggregation and alterations in RNA processing and quality control can disrupt protein import[86].

557 More recently, defects in mitochondrial protein import have also been connected to impaired

558 proteostasis[87]. Mutant HTT can also disrupt mitochondrial trafficking and impair ATP production

559 prior to the appearance of detectable mHTT aggregates[88,89]. The N17 domain is required for HTT

560 subcellular localization to mitochondria[43,88,89] and the interaction of HTT with the protein import

561 complex TIM23 requires both the N17 and polyQ regions of HTT[47]. Intriguingly, mHTT localizes

562 within the intermembrane space in mitochondria and is more strongly associated with TIM23

563 than WT HTT, potentially blocking import of nuclear-encoded mitochondrial proteins[48]. This

564 suggests a potential mechanism (**Fig. 10**) underlying the aberrant structures we observe in HD

565 mitochondria (including enlarged granules), particularly for dN17-BACHD, where normal HTT

566 function is impaired by both the lack of the N17 domain and the expansion of the polyQ

567 tract[34,47,54].

568 The sheet aggregates we observed here within autophagic organelles appear to be another early

569 structural hallmark of HD since they were consistently present in the neurites of all HD model

570 systems we examined. In addition to cryoET tomograms, we also collected high-magnification

571 cryoEM images of sample areas with sheet aggregates; the lack of evidence for periodic

572 arrangement in them by Fourier analysis suggests that they are not classical amyloid filaments

573 with the known characteristic cross-beta sheet structures perpendicular to the filament axis[90];

574 however, this may not be surprising since it is possible that the sheet aggregates we observed

575 may not contain fibrillar mHTT, and HD does not strictly fit within the diseases known as

576 amyloidoses[91]. It is also possible that future purification of the sheet aggregates may render them

577 more amenable to increasingly clarifying high-resolution analyses without interference from the

578 cell membrane and surrounding milieu of the crowded cytosol. Whether the sheet aggregates

579 contain mHTT also awaits future biochemical analyses of purified autophagic organelles and/or

580 degenerated mitochondrial particles. Nevertheless, our data here suggest that these unusual

581 structural features, likely in components of autophagic pathways, are a consequence of the stress

582 and toxicity induced by the presence of full-length, endogenous mHTT or fragments derived from

583 it.

584
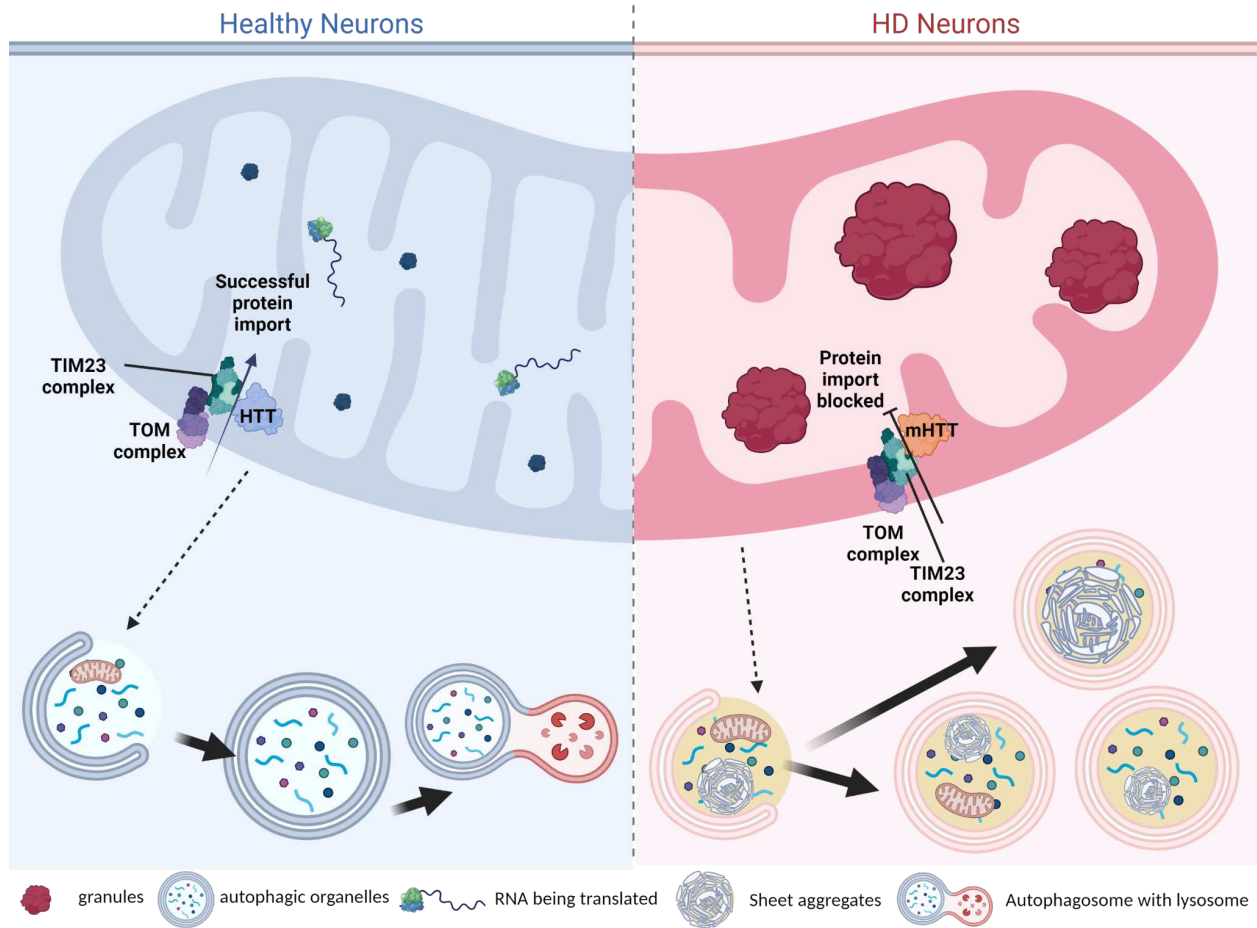
Fig. 10. **Proposed mechanism of aberrant mitochondrial structures and sheet aggregates in autophagic organelles.** Our work here highlights the accumulation of enlarged mitochondrial granules in four human and two mouse HD neuronal models, which we hypothesize could be composed of calcium phosphate and/or enlarged mitochondrial RNA granules that may result from disrupted protein import due to mHTT's abnormal interaction with the TIM23 complex[48]. Additionally, our mass spectrometry data suggests that RNA binding may be disrupted within HD mitochondria, which may lead to excess RNA molecules within the mitochondrial matrix. There is cross talk between mitochondria, autophagosomes, and lysosomes, and dysfunctional mitochondria are packaged by mitophagy, in addition to other cellular waste; *i.e.*, proteins shown within the autophagic organelles. In healthy neurons, we observe a normal autophagy cascade while in HD we observe accumulation of sheet aggregates in autophagic organelles, which are likely to not be as efficiently processed for degradation as expected in healthy and WT neurons, even though we often see them associated to lysosomes. (Created in BioRender.com).

Given the potential hypotheses suggested by the observation that the sheet aggregates may be degenerated mitochondria (**Supplementary Fig. 3e,f**) associated with lysosomes (**Supplementary**

600 **Fig. 3g**), it would be expected that instances of mitochondria that simultaneously exhibit some

601 recognizable cristate, cristae junctions, and granules, at the same time as some clear sheet

602 aggregate densities, might constitute extremely rare events that are hard to capture along a

603 dynamic degeneration process. That is, the sheet aggregates may develop from remodeled and

604 compromised mitochondrial membranes and/or granules through a previously unresolved

605 mechanism in HD cells endogenously expressing untagged mHTT, and may go through

606 intermediate states where mitochondrial features are extremely challenging to recognize or no

607 longer present due to degeneration, before the overt appearance of sheet aggregate densities

608 within them. Indeed, we observed many double membrane-bound compartments in most of our

609 specimens whose identities were not clearly assignable but that may actually correspond to

610 mitochondria in these hypothesized intermediate states, such as the organelle in the bottom left

611 of **Supplementary Fig. 3e,** and those in **Supplementary Fig. 3a-d**. In support of this hypothesis,

612 mitochondria have been recently demonstrated to interact directly with lysosomes via their

613 membranes[53]. Indeed, the traditional paradigm for largely separate functions by these two

614 organelles has changed with emerging evidence that mitochondria and lysosomes are mutually

615 functional and interdependent, with profound implications to the underpinnings of aging[92] and

616 neurodegeneration[93,94].

617 In spite of the challenges, this exciting observation provides an additional hint into resolving the

618 potential origin of the sheet aggregates. Mitochondrial autophagy (mitophagy) is a clearance

619 mechanism of defective mitochondria via autophagy[35] and is altered in many neurodegenerative

620 disorders such as Parkinson disease (PD) and Alzheimer disease (AD)[95]. There is now emerging

621 evidence that mitophagy is also defective in HD. Altered mitophagy may also potentially

622 contribute to the bioenergetic deficits observed in various HD models[13,96] and at least in part to

623 the excessive weight loss that is characteristic of late-stage human HD[97,98]. Consistent with our

624 findings, recent work[31] has identified non-fibrillar mHTT within single-membrane-bound

625 organelles in cortical and striatal tissue from zQ175 HD mice, including multivesicular bodies

626 (MVB) and amphisomes, using correlative light and conventional electron microscopy of samples

627 fixed by freeze substitution. The localization of non-fibrillar mHTT changed depending on the

628 disease stage, with presymptomatic stages showing localization within MVBs/amphisomes and

629   late stage disease showing localization to the autolysosomes or residual bodies[31]. Our findings

630   here in intact, cryo-preserved human patient and mouse model-derived neurons are suggestive

631   of even earlier events and thus are likely complementary.

632   Our previous studies showed improved synaptic-associated gene expression and mitochondrial

633   DNA integrity in HD iPSC-neurons after PIAS1 KD[36,65]. Based on these data, we evaluated the

634   effect of reduced PIAS1 levels on the mitochondrial and autophagosome structural phenotypes

635   in HD patient iPSC- and mouse model-derived neurons and observed rescue of these phenotypes

636   in the former and partial rescue in the latter (**Fig. 8 & 9**). Interestingly, our findings on PIAS1 KD

637   also inform on the possible biochemical composition of mitochondrial granules. For example, we

638   previously identified MCUR1, CALM1, CALB1 and CABP1 as differentially expressed in iPSC-

639   derived neurons upon *PIAS1* knockdown[65], consistent with changes to calcium phosphate

640   granules. We also observed alterations in the levels of RNA binding and processing genes,

641   consistent with changes to mitochondrial RNA granules. Several mitochondrial proteins are

642   SUMO modified (identified in yeast) and require Siz1 or Siz2 for modification (*i.e.*, PIAS1/2)[99]. For

643   instance, Fis1, involved in mitophagy, is SUMO modified and reduction of SUMO modification of

644   Fis1 restores appropriate mitophagy in Hela cells[100]. Finally, a recent report identified PIAS1 as a

645   potential age-of-onset modifier. PIAS1 containing a S510G single nucleotide polymorphism,

646   which reduces SUMO modification of mHTT[101], delays HD onset and produces milder disease

647   severity in HD mice, consistent with the concept that reduced PIAS1 levels may ameliorate

648   disease. Our studies thus represent a proof of concept that the synergistic combination of cryoET

649   and proteomics of iPSC- and mouse model-derived neurons or organelles within them can inform

650   on the impact of a given therapeutic strategy on structural features and ultimately function, and

651   may be applicable to other cellular systems and disease models.

652

653   **METHODS**

654   **Ethics Statement and mouse models**

30

655 All protocols involving the use of animals in the study, namely BACHD[32] and deltaN17 BACHD[33],

656 were approved by the Institutional Animal Care and Use Committee at the University of California

657 in San Diego.

658

659 **iPSC culture, differentiation, and maintenance**

660 Neuronal differentiation was performed once iPSC colonies reached 60-70% confluency as

661 previously described[4]. Differentiation was initiated by washing iPSC colonies with phosphate

662 buffered saline pH 7.4 (PBS – Gibco) and switching to SLI medium (Advanced DMEM/F12 (1:1)

663 supplemented with 2 mM Glutamax™ (Gibco), 2% B27 without vitamin A (Life technologies), 10

664 µM SB431542, 1 µM LDN 193189 (both Stem Cell Technologies), 1.5 µM IWR1 (Tocris)) with daily

665 medium changes. This was day 0 of differentiation; at day 4, cells were pretreated with 10 µM

666 Y27632 dihydrochloride (Tocris) and then washed with PBS and then passaged 1:2 with StemPro

667 Accutase (Invitrogen) for 5 minutes at 37 °C and replated onto plates which were coated with

668 hESC qualified matrigel (1 hour at 37 °C) in SLI medium containing 10 µM Y27632 dihydrochloride

669 for 1 day after plating and continued daily feeding with SLI medium until day 8. At day 8, cells

670 were passaged 1:2 as above and replated in LIA medium (Advanced DMEM/F12 (1:1)

671 supplemented with 2 mM Glutamax™, 2% B27 without vitamin A, 0.2 µM LDN 193189, 1.5 µM

672 IWR1, 20 ng/ml Activin A (Peprotech)) with 10 µM Y27632 dihydrochloride for 1 day after plating

673 and daily feeding was continued through day 16. At day 16, cells were plated on either the carbon

674 side of Quantifoil holey carbon film grids (Electron Microscopy Sciences; see below for grid

675 preparation for cryoET), or in 6 well Nunclon coated plates with PDL and hESC matrigel for

676 mitochondrial isolation. Cells were plated at 1x10^6 for mitochondrial isolation and at half density

677 for cryoET of neurites in intact neurons at 500,000 per dish on the 35 mm Mat-tek glass bottomed

678 dish containing 3 holey-carbon grids in SCM1 medium (Advanced DMEM/F12 (1:1) supplemented

679 with 2 mM Glutamax™, 2% B27 (Invitrogen), 10 µM DAPT, 10 µM Forskolin, 300 µM GABA, 3 µM

680 CHIR99021, 2 µM PD 0332991 (all Tocris), to 1.8 mM CaCl$_2$, 200 µM ascorbic acid (Sigma-Aldrich),

681 10 ng/ml BDNF (Peprotech)). Cells on EM grids were topped up with an additional 1 ml of SCM1

682 (35 mm Mat-Tek dishes). We tried even lower densities to improve the probability of getting one

683 cell per grid square; however, the neurons did not survive or did not differentiate well. Medium

31

684   was 50% changed every 2-3 days. On day 23, medium was fully changed to SCM2 medium

685   (Advanced DMEM/F12 (1:1): Neurobasal A (Gibco) (50:50) supplemented with 2 mM

686   Glutamax[TM]), 2% B27, to 1.8 mM $CaCl_2$, 3 µM CHIR99021, 2 µM PD 0332991, 200 µM ascorbic

687   acid, 10 ng/ml BDNF) and 50% medium changes were subsequently performed every 2-3 days.

688   Cells were considered mature and ready for subsequent analyses and experiments at day 37.

689   **Mouse model neuronal culture and maintenance**

690   Established protocols were followed to set up cortical neurons collected from mouse E18

691   embryos [102,103,104]. Briefly, cortical tissues were extracted from E18 mouse embryos and

692   extensively rinsed in HBSS with 1% Penicillin-Streptomycin, followed by dissociation in 0.25%

693   trypsin with 1 mg/ml DNase I. Cortical neurons were isolated and plated with plating media

694   (Neurobasal with 10% FBS, 1xB27,1xGlutaMAX) onto either glass coverslips for immunostaining

695   or into 12 well plates for biochemistry at appropriate density. Both the cover glasses and plates

696   were pre-coated with poly-L-lysine (Invitrogen). Plating medium was replaced with a

697   maintenance medium (Neurobasal, 1xB27, 1xGlutaMAX) the following day. Only 2/3 of the media

698   was replaced every other day until the conclusion of the experiments.

699   **Mitochondria isolation**

700   Day 37 neurons were harvested using the Miltenyi MACS human mitochondria isolation kit

701   (Miltenyi Biotec 130-094-532) with additional proteases added to the lysis buffer aprotinin (10

702   µg/ml), leupeptin (10 µg/ml), PMSF (1 mMl), EDTA-free protease inhibitor cocktail III (1x SIgma-

703   Aldrich - 539134) at a concentration of 10 million/ml of lysis buffer and disruption was performed

704   using an 27 G needle using a syringe to triturate 10 times up and down and then proceeding to

705   labeling following the manufacturer's recommended protocol. Final mitochondrial pellet was

706   resuspended in 50 µl of storage buffer and flash frozen in liquid nitrogen, stored at -80 °C until

707   mass spec analysis.

708   **RNA extraction & concentration**

709   RNA extraction was performed using QIAGEN RNEasy kit following manufacturer's protocol. RNA

710   was eluted in 50 μl of nuclease free H_2O and required further concentration for cDNA synthesis.

711   RNA concentration was performed using ZYMO RNA Clean and Concentrator™-5 kit.

712   **cDNA synthesis**

713   100 ng of RNA was used for cDNA synthesis using the Quantabio qScript® cDNA SuperMix kit

714   while 25 ng of the RNA was used for RT-reaction of just RNA and nuclease-free water. cDNA

715   synthesis was performed using the manufacturer's protocol at 25 °C for 5 minutes, then 42 °C for

716   30 minutes, and finally 85 °C for 5 minutes in a Bio-Rad T100 thermal cycler.

717   **qRT-PCR**

718   One μl of cDNA at a concentration of 5 ng/μl was used per reaction, with 10 μM primers for

719   mouse *Pias1* and *Eif4a2* for a housekeeping control using previously published primers[65].

720   Quantification was performed on a Quantstudio 5 using SYBR green reagent (Biorad) running

721   delta delta CT method and calculating fold change normalizing to non-transgenic primary

722   neurons control SMARTPool siRNA. Prism 9.0 was used to calculate statistical significance by two

723   way ANOVA.

724   **Western blot**

725   Protein was harvested from frozen cell pellets (for CRISPR validation of the clone) using RIPA lysis

726   buffer or from isolated mitochondria samples described above. Samples were subjected to SDS

727   (sodium dodecyl sulfate) polyacrylamide gel electrophoresis and Western blotting onto

728   nitrocellulose. Membranes were assessed using either infrared fluorescence on the Li-Cor.

729   Antibodies were as follows: LC3ab (Cell Signaling #12741), PIAS1 (Cell Signaling #3550), CTIP2

730   (abcam #ab18465), ATPB (abcam #ab14730), normalization of loading was calculated based on

731   REVERT total loading stain.

732   **Immunofluorescence**

733   Immunofluorescence staining on day 37 neurons was performed as previously described[4]

Pias1 knockdown in neurons

Knockdown of *Pias1* was performed for mouse model neurons using Accell SMARTPool siRNA against *Pias1* (Horizon Discovery cat#E-059344-00-0005) and a non-targeting SMARTPool control (Horizon Discovery cat#D-001910-10-05) for comparison. Treatment was performed at 3 days *in vitro* (DIV3) at a concentration of 1 μM in 1 ml of medium per 35 mm MatTek dish, medium was topped up to 2 ml after 24 hours and then 2/3 of the media was replaced every other day until the conclusion of the experiments.

CRISPR-Cas9 heterozygous knockout of PIAS1 in iPSC

Clones were selected from stem cell edited pools in a method that was previously described[65]

Grid preparation for cryoET of HD patient iPSC-derived neurons and mouse model neurons

For iPSCs, Quantifoi®l R 2/2 Micromachined Holey Carbon grid: 200 mesh gold (SPI supplies Cat#:4420G-XA) grids were prepared for cell plating by sterilizing using forceps to carefully submerge them in 100% ethanol (Fisher Scientific) at an angle perpendicular to the liquid surface and then passed quickly through a yellow flame. Grids were then placed into 1 ml of poly-D-lysine (100 μg/ml in borate buffer, pH 8.4) in a 35 mm Mat-Tek glass coverslip bottom dish (VWR P35G-0-14-C) at an angle perpendicular to the liquid's surface, and coated on the bottom of the dish for at least 1 hour at room temperature. When cells were ready for plating, the grids were washed two times with sterile-filtered Milli-Q H_2O and a final wash with PBS before cell plating.

For mouse neurons, EM grids were briefly dipped into 70% ETOH to sterilize, followed by coating with 0.1mg/ml PDL[105]. The grids were rinsed with sterile dH_2O and loaded with isolated neurons. The maintenance of these grids were exactly as described above. DIV14 neurons were used for cryoEM/cryoET experiments .

For both iPSC-derived and mouse model neurons, cells grown on grids were vitrified using the temperature- and humidity-controlled Leica GP2. Grids were retrieved from culture dishes using the forceps for the Leica device, and 3 μl of 15 nm BSA gold tracer (Fisher Scientific; Catalog

759   No.50-248-07) was pipetted onto the carbon- and cell-side of the grid. Grids were loaded and

760   blotted for 5 seconds in 95% humidity at 37 °C and immediately plunged into liquid propane. The

761   vitrified grids were transferred into grid storage boxes in clean liquid nitrogen and then stored in

762   clean liquid nitrogen prior to cryoET imaging.

763   Cells on the remainder of the dishes that were used for cryoET, were scraped using a cell scraper

764   in cold PBS and pelleted at 350 xg for 5 minutes, PBS was aspirated and the pellets were flash-

765   frozen in liquid nitrogen and stored at -80 °C for later analysis of knockdown.

766   **CryoEM/ET data collection**

767   For each specimen, namely vitrified HD patient iPSC-derived and mouse primary neurons, we

768   collected low magnification (6500X) cryogenic TEM images and assembled them into montages

769   to screen for regions of interest (ROI) before cryoET tilt series collection. All images were acquired

770   using a G3 Titan Krios[TM] cryo-electron microscope (ThermoFisher Scientific) operated at 300 kV,

771   energy filter at 30 eV, in low-dose mode using SerialEM software[106]. At each tilt angle, we

772   recorded "movies'' with 5-6 frames per movie using a Gatan K2[TM] or K3[TM] direct electron

773   detection camera with a BioQuantum[TM] Imaging Filter (Gatan, Inc). The tilt series were collected

774   at higher magnification (39000X, 3.47 Å/pixel sampling size) using a dose-symmetric tilting

775   scheme[107] from 0°, target defocus of −5 μm and a cumulative dose of ~120 e/Å[2].

776   **Tomographic reconstruction**

777   Upon data collection, all tilt series were automatically transferred to our computing and storage

778   data clusters and images were motion-corrected using MotionCor2[108] and reconstructed into full

779   tomograms automatically using EMAN2[109]. This on-the-fly reconstruction facilitated the

780   screening of tomograms.

781   After screening the automated cryoET reconstructions, we used IMOD[110] software for standard

782   weighted-back projection tomographic reconstruction of tomograms with interesting and

783   relevant features, using coarse cross-correlation-based alignment, gold fiducial-based

784   alignment, or patch tracking alignment. For each tilt series, unsuitable images with large drift,

785   excessive ice contamination, etc. were manually removed prior to tilt series alignment. For

786   cryoET tilt series containing prominent sheet aggregates and subjected to Fourier analysis and

787   subtomogram averaging attempts to determine whether they contained repeating features, we

788   corrected for the contrast transfer function (CTF) using IMOD's recent 3D-CTF correction

789   algorithm and reconstructed using a SIRT-like filter (16 iterations)(**Fig. 4** and **Supplementary Fig.**

790   **3**).

Tomographic annotation and segmentation

791

792   The tomograms containing mitochondrial granules were post-processed binning by 4x and

793   applying various filters, such as a low-pass Gaussian filter at a frequency=0.01, a Gaussian high-

794   pass filter to dampen the first 1-5 Fourier pixels, normalization, and thresholding at 3 standard

795   deviations away from the mean. For both types of tomograms (containing mitochondrial granules

796   or sheet aggregates), we carried out tomographic annotation of different features in binned-by-

797   4 tomograms using the EMAN2 semi-automated 2D neural network-based annotation[42], and

798   performed manual clean-up of false positives in UCSF Chimera[111]. The cleaned-up annotations

799   were thresholded, low-pass filtered, and turned into binary masks, which were multiplied by

800   contrast-reversed versions of the tomograms to segment out each corresponding feature.

Visualization of tomograms containing sheet aggregates

801

802   Initially, the sheet aggregates appeared filamentous in 2D z-slices through our cryoET

803   tomograms. When attempts at subtomogram averaging failed to yield averages with filamentous

804   morphology, and instead resulted in featureless sheets, we more carefully examined the

805   tomograms slice-by-slice to understand the causes for this apparent failure. This revealed that

806   the linear features in a section persisted through multiple sections above or below. While this

807   might be expected due to lower resolvability in z because of the missing wedge, we also noticed

808   that the linear features shifted their location from section to section (as if drifting sideways), and

809   in different directions. This anomaly suggested that the linear features seen in 2D slices

810   corresponded to sheets in 3D, oriented at various angles with respect to the x-y plane, and

811   explained the preliminary exploratory subtomogram averages that had also revealed a sheet

812   morphology.

813   The sheets seem to be composed of extremely electron dense materials yielding high contrast in

814   cryoEM/ET images, and are exceedingly thin (~20 Å , a bit more or less in some regions), as

815   measured from 3D-CTF corrected tomograms without any downsampling or low-pass filtration.

816   **Quantification and statistical analysis of mitochondria granules size.**

817

818   We developed a two-stage deep learning system for voxel level annotation of mitochondria and

819   granules in tomograms. In the first stage, our system is trained on a handful of annotated slices

820   on a subset of tomograms and learns to segment mitochondria and granules. In the second stage,

821   we use our model to make predictions on all the tomograms and use high confidence predictions

822   as pseudo-annotations to augment our training set. We then train a new model on this

823   augmented training set and use its predictions to quantify the number and sizes of mitochondria

824   and granules in the tomograms.

825   In the first stage, we train a 3D-UNet[112] model to perform segmentation of the 3D volumes

826   containing objects of interest. We train two separate models, one for segmenting mitochondria

827   and the other for segmenting granules. These models are trained in a semi-supervised fashion on

828   sparsely annotated 3D volumes - only 2% of the 2D slices are manually annotated with each pixel

829   being labeled as being part of the background or being part of the mitochondria / granule.

830   Since annotating each slice is a time-consuming process, we utilize pseudo-labelling to generate

831   more annotations. In the second stage, we run every tomogram through our model and add the

832   high confidence predictions to the training set. Next, we retrain our model on the expanded

833   training set which consists of both human- and machine (pseudo)-labeled slices. The new model

834   is then used to make the final voxel level predictions on all the tomograms.

835   We refine the 3D segmentations in the post-processing stage. We run a connected components

836   analysis to count the number of segmented objects. We filter out background noise in the

837   predictions by discarding objects which don't fall within the expected range of volumes. We

838 retain granule detections which are located within a detected mitochondrion. After post-
839 processing, we scale each voxel by a factor of 21.02 to get the volume in nm^3.

840 Compilation of the data into graphs was performed in Prism 9.3
841 (https://www.graphpad.com/scientific-software/prism/) with statistics performed based on the
842 number of groups to compare and data normality. iPSC-derived neurons used Dunn's multiple
843 comparisons to compare control to the various HD lines, for the mouse primary neurons, Dunn's
844 multiple comparisons were used to compare WT vs all other groups and then BACHD vs dN17
845 and Control siRNA vs *Pias1* siRNA treatment.

846 **Sample preparation for proteomic analysis**

847 Isolated mitochondria were solubilized in a final concentration of 1% SDS and mitochondrial
848 proteome was extracted using methanol-chloroform precipitation. 400 µl methanol, 100 µl
849 chloroform and 350 µl water were added sequentially to each 100 µl sample, followed by
850 centrifugation at 14,000 x g for 5 min at room temperature. The top phase was removed and the
851 protein interphase was precipitated by addition of 400 µl methanol, followed by centrifugation
852 at 14,000 g for 5 min at room temperature. Pellet was air dried and resuspended in 8M urea, 25
853 mM ammonium bicarbonate (pH 7.5). Protein concentration was determined by BCA (Thermo
854 Fisher) and 2-4 µg total protein were subjected to reduction and alkylation by incubation with 5
855 mM DTT for 1 h at room temperature followed by 5 mM iodoacetamide for 45 min at room
856 temperature, in the dark. The samples were then incubated with 1:50 enzyme to protein ratio of
857 sequencing-grade trypsin (Promega) overnight at 37 °C. Peptides were acidified with
858 trifluoroacetic acid to a final concentration of 1%, desalted with µC18 Ziptips (Millipore Sigma),
859 dried and resuspended in 10 µL 0.1% formic acid in water.

860 **LC-MS/MS acquisition**

861 LC-MS/MS analyses were conducted using a QExactive Plus Orbitrap (QE) mass spectrometer
862 (Thermo Fisher) coupled online to a nanoAcquity UPLC system (Waters Corporation) through an
863 EASY-Spray nanoESI ion source (Thermo Fisher). Peptides were loaded onto an EASY-Spray

864 column (75 μm x 15 cm column packed with 3 μm, 100 Å PepMap C18 resin) at 2% B (0.1% formic

865 acid in acetonitrile) for 20 min at a flow rate of 600nl/min. Peptides were separated at 400 nL/min

866 using a gradient from 2% to 25% B over 48 min (QE) followed by a second gradient from 25% to

867 37% B over 8 minutes and then a column wash at 75% B and reequilibration at 2% B. Precursor

868 scans were acquired in the Orbitrap analyzer (350-1500 m/z, resolution: 70,000@200 m/z, AGC

869 target: 3×10^6). The top 10 most intense, doubly charged or higher ions were isolated (4 m/z

870 isolation window), subjected to high-energy collisional dissociation (25 NCE), and the product

871 ions measured in the Orbitrap analyzer (17,500@200 m/z, AGC target: 5e4).

872 **Mass spectrometry data processing**

873 Raw MS data were processed using MaxQuant version 1.6.7.0 (Cox and Mann, 2008). MS/MS

874 spectra searches were performed using the Andromeda search engine[113] against the forward and

875 reverse human and mouse Uniprot databases (downloaded August 28, 2017 and November 25,

876 2020, respectively). Cysteine carbamidomethylation was chosen as fixed modification and

877 methionine oxidation and N-terminal acetylation as variable modifications. Parent peptides and

878 fragment ions were searched with maximal mass deviation of 6 and 20 ppm, respectively. Mass

879 recalibration was performed with a window of 20 ppm. Maximum allowed false discovery rate

880 (FDR) was <0.01 at both the peptide and protein levels, based on a standard target-decoy

881 database approach. The "calculate peak properties" and "match between runs" options were

882 enabled.

883 All statistical l tests were performed with Perseus version 1.6.7.0 using either ProteinGroups or

884 Peptides output tables from MaxQuant. Potential contaminants, proteins identified in the

885 reverse dataset and proteins only identified by site were filtered out. Intensity-based absolute

886 quantification (iBAQ) was used to estimate absolute protein abundance. Two-sided Student's *t*-

887 test with a permutation-based FDR of 0.01 and S0 of 0.1 with 250 randomizations was used to

888 determine statistically significant differences between grouped replicates. Categorical

889 annotation was based on Gene Ontology Biological Process (GOBP), Molecular Function (GOMF)

890 and Cellular Component (GOCC), as well as protein complex assembly by CORUM.

891 Additional analysis was performed on all potential identities of the differentially

892 enriched/depleted proteins that were significant by t-test, using Panther pathways and Panther

893 Overrepresentation algorithms for GO Molecular Function, GO Biological Processes and GO

894 Cellular Component at http://www.pantherdb.org/. Ingenuity Pathway Analysis was performed

895 using the significantly differential proteins to assess pathways, networks and upstream

896 regulators. For comparison of DEPs to PIAS1 knockdown DEGs, overlap statistics for

897 overrepresentation was performed at http://nemates.org/MA/progs/overlap_stats.html using

898 total genome number of genes at 20,500.

899

909

910

911 **AUTHOR CONTRIBUTIONS**

912

913 G-H.W., C.S-G., J.G.G-M., P.M., L.M.J., M.F.S, C.W., W.M., J.F., L.M.T., & W.C. were involved in

914 conception and design of the experiments related to differentiation and cryo electron

915 tomography.

916 G-H.W., J.G.G-M., M.F.S., &W.C. analyzed cryo-ET data.

917 C.S-G., optimized iPSC cell growth on EM grids, and performed all iPSC differentiations and cell

918 culture.

919 Y.G., performed all mouse model neuronal cultures.

920   G-H.W., L.M.J., & P.M. optimized cryoET grid preparation and screening and collected all cryoET
921   data.
922   J.G.G-M. & G-H.W. performed tilt series alignment and tomographic reconstruction.
923   J.G.G-M., G-H.W., and C.D. performed tomographic annotation.
924   J.G.G-M., G-H.W., & M.F.S. participated in cryoET data visualization.
925   C.S-G, R.A., J.F., and L.M.T. were involved in conception and design of the experiments for the
926   mitochondria mass spectrometry.
927   C.S-G, R.A., N.R.G., and L.M.T. were involved in the acquisition, the validation, the analysis and
928   interpretation of the mitochondrial mass spectrometry data.
929   C.S-G., Y.G., R.M., and K.Q.W. were involved in the differentiation and cell culture of the neurons
930   and validation of PIAS1 knockdown.
931   S.G., J.H. & S.Y were involved in creating an artificial intelligence-based algorithm for automated
932   segmentation of features in cryoET tomograms and quantitative analyses of mitochondrial
933   granules.
934   G-H.W., J.G.G-M., & C.D. were involved in extensive manual reference labeling to train artificial
935   intelligence algorithms for segmentation and quantification of features in cryoET tomograms.
936   G-H.W, C.S-G, J.G.G-M., R.A., C.W., S.G., S.Y., L.M.T. & W.C, wrote the manuscript.
937   G-H.W, C.S-G, J.G.G-M., M.F.S., L.M.T. & W.C., substantively revised the manuscript with input
938   from all authors.
939
940
941   **DATA AVAILABILITY**
942   We will deposit representative tomograms for each phenotype in EMDB
943   (https://www.emdataresource.org/deposit.html); and in Chorus, for proteomics.
944
945
946
947
948
949
950

REFERENCES

951

952   1.   The Huntington's Disease Collaborative Research Group. A novel gene containing a
953   trinucleotide repeat that is expanded and unstable on Huntington's disease chromosomes.
954   *Cell* **72**, 971–983 (1993).

955   2.   Walker, F. O. Huntington's disease. *Lancet* **369**, 218–228 (2007).

956   3.   Nance, M. A. & Myers, R. H. Juvenile onset Huntington's disease?clinical and research
957   perspectives. *Mental Retardation and Developmental Disabilities Research Reviews* vol. 7
958   153–157 (2001).

959   4.   Smith-Geater, C. *et al.* Aberrant Development Corrected in Adult-Onset Huntington's
960   Disease iPSC-Derived Neuronal Cultures via WNT Signaling Modulation. *Stem Cell Reports*
961   **14**, 406–419 (2020).

962   5.   Waldvogel, H. J., Kim, E. H., Tippett, L. J., Vonsattel, J.-P. G. & Faull, R. L. M. The
963   Neuropathology of Huntington's Disease. *Curr. Top. Behav. Neurosci.* **22**, 33–80 (2015).

964   6.   Takahashi, K. & Yamanaka, S. Induction of pluripotent stem cells from mouse embryonic and
965   adult fibroblast cultures by defined factors. *Cell* **126**, 663–676 (2006).

966   7.   Takahashi, K. *et al.* Induction of pluripotent stem cells from adult human fibroblasts by
967   defined factors. *Cell* **131**, 861–872 (2007).

968   8.   Hamazaki, T., El Rouby, N., Fredette, N. C., Santostefano, K. E. & Terada, N. Concise Review:
969   Induced Pluripotent Stem Cell Research in the Era of Precision Medicine. *Stem Cells* **35**, 545–
970   550 (2017).

971   9.   HD iPSC Consortium. Developmental alterations in Huntington's disease neural cells and
972   pharmacological rescue in cells and mice. *Nat. Neurosci.* **20**, 648–660 (2017).

973   10. HD iPSC Consortium. Induced pluripotent stem cells from patients with Huntington's disease
974   show CAG-repeat-expansion-associated phenotypes. *Cell Stem Cell* **11**, 264–278 (2012).

975   11. Ring, K. L. *et al.* Genomic Analysis Reveals Disruption of Striatal Neuronal Development and
976   Therapeutic Targets in Human Huntington's Disease Neural Stem Cells. *Stem Cell Reports* **5**,
977   1023–1038 (2015).

978   12. Delli Carri, A. *et al.* Developmentally coordinated extrinsic signals drive human pluripotent
979   stem cell differentiation toward authentic DARPP-32+ medium-sized spiny neurons.
980   *Development* **140**, 301–312 (2013).

981   13. HD iPSC Consortium. Bioenergetic deficits in Huntington's disease iPSC-derived neural cells
982   and rescue with glycolytic metabolites. *Hum. Mol. Genet.* **29**, 1757–1771 (2020).

983   14. Barnat, M. *et al.* Huntington's disease alters human neurodevelopment. *Science* **369**, 787–
984   793 (2020).

985   15. Lemprière, S. Huntington disease alters early neurodevelopment. *Nat. Rev. Neurol.* **16**, 459
986   (2020).

987   16. Liu, K.-Y. *et al.* Disruption of the nuclear membrane by perinuclear inclusions of mutant

988　huntingtin causes cell-cycle re-entry and striatal cell death in mouse and cell models of
989　Huntington's disease. *Hum. Mol. Genet.* **24**, 1602–1616 (2015).

990　17.　Grima, J. C. *et al.* Mutant Huntingtin Disrupts the Nuclear Pore Complex. *Neuron* vol. 94 93–
991　107.e6 (2017).

992　18.　Koyuncu, S. *et al.* The ubiquitin ligase UBR5 suppresses proteostasis collapse in pluripotent
993　stem cells from Huntington's disease patients. *Nat. Commun.* **9**, 2886 (2018).

994　19.　Carty, N. *et al.* Characterization of HTT inclusion size, location, and timing in the zQ175
995　mouse model of Huntington's disease: an in vivo high-content imaging study. *PLoS One* **10**,
996　e0123527 (2015).

997　20.　Davies, S. W. *et al.* Formation of neuronal intranuclear inclusions underlies the neurological
998　dysfunction in mice transgenic for the HD mutation. *Cell* **90**, 537–548 (1997).

999　21.　DiFiglia, M. *et al.* Aggregation of huntingtin in neuronal intranuclear inclusions and
1000　dystrophic neurites in brain. *Science* **277**, 1990–1993 (1997).

1001　22.　Sieradzan, K. A. *et al.* Huntington's disease intranuclear inclusions contain truncated,
1002　ubiquitinated huntingtin protein. *Exp. Neurol.* **156**, 92–99 (1999).

1003　23.　Ochaba, J. *et al.* Potential function for the Huntingtin protein as a scaffold for selective
1004　autophagy. *Proc. Natl. Acad. Sci. U. S. A.* **111**, 16889–16894 (2014).

1005　24.　Nekrasov, E. D. *et al.* Manifestation of Huntington's disease pathology in human induced
1006　pluripotent stem cell-derived neurons. *Mol. Neurodegener.* **11**, 27 (2016).

1007　25.　Guo, Q. *et al.* The cryo-electron microscopy structure of huntingtin. *Nature* **555**, 117–120
1008　(2018).

1009　26.　Galaz-Montoya, J. G., Shahmoradian, S. H., Shen, K., Frydman, J. & Chiu, W. Cryo-electron
1010　tomography provides topological insights into mutant huntingtin exon 1 and polyQ
1011　aggregates. *Commun Biol* **4**, 849 (2021).

1012　27.　Gruber, A. *et al.* Molecular and structural architecture of polyQ aggregates in yeast.
1013　*Proceedings of the National Academy of Sciences* vol. 115 E3446–E3453 (2018).

1014　28.　Bäuerlein, F. J. B. *et al.* In Situ Architecture and Cellular Interactions of PolyQ Inclusions. *Cell*
1015　**171**, 179–187.e10 (2017).

1016　29.　Shahmoradian, S. H. *et al.* TRiC's tricks inhibit huntingtin aggregation. *Elife* **2**, e00710 (2013).

1017　30.　Darrow, M. C. *et al.* Structural Mechanisms of Mutant Huntingtin Aggregation Suppression
1018　by the Synthetic Chaperonin-like CCT5 Complex Explained by Cryoelectron Tomography. *J.*
1019　*Biol. Chem.* **290**, 17451–17461 (2015).

1020　31.　Zhou, Y. *et al.* Correlative light and electron microscopy suggests that mutant huntingtin
1021　dysregulates the endolysosomal pathway in presymptomatic Huntington's disease. *Acta*
1022　*Neuropathol Commun* **9**, 70 (2021).

1023　32.　Gray, M. *et al.* Full-length human mutant huntingtin with a stable polyglutamine repeat can
1024　elicit progressive and selective neuropathogenesis in BACHD mice. *J. Neurosci.* **28**, 6182–
1025　6195 (2008).

1026   33. Gu, X. *et al.* N17 Modifies mutant Huntingtin nuclear pathogenesis and severity of disease
1027   in HD BAC transgenic mice. *Neuron* **85**, 726–741 (2015).
1028   34. Sharma, A., Behl, T., Sharma, L., Aelya, L. & Bungau, S. Mitochondrial Dysfunction in
1029   Huntington's Disease: Pathogenesis and Therapeutic Opportunities. *Curr. Drug Targets* **22**,
1030   1637–1667 (2021).
1031   35. Hwang, S., Disatnik, M.-H. & Mochly-Rosen, D. Impaired GAPDH-induced mitophagy
1032   contributes to the pathology of Huntington's disease. *EMBO Mol. Med.* **7**, 1307–1326
1033   (2015).
1034   36. Ochaba, J. *et al.* PIAS1 Regulates Mutant Huntingtin Accumulation and Huntington's
1035   Disease-Associated Phenotypes In Vivo. *Neuron* **90**, 507–520 (2016).
1036   37. Blancard, C. & Salin, B. Plunge Freezing: A Tool for the Ultrastructural and
1037   Immunolocalization Studies of Suspension Cells in Transmission Electron Microscopy. *J. Vis.*
1038   *Exp.* (2017) doi:10.3791/54874.
1039   38. Plunge Freezing for Electron Cryomicroscopy. in *Methods in Enzymology* vol. 481 63–82
1040   (Academic Press, 2010).
1041   39. Shen, K. *et al.* Control of the structural landscape and neuronal proteotoxicity of mutant
1042   Huntingtin by domains flanking the polyQ tract. *eLife* vol. 5 (2016).
1043   40. Nazarov, S., Chiki, A., Boudeffa, D. & Lashuel, H. A. The structural basis of huntingtin (Htt)
1044   fibril polymorphism, revealed by cryo-EM of exon 1 Htt fibrils. *bioRxiv* 2021.09.23.461534
1045   (2021) doi:10.1101/2021.09.23.461534.
1046   41. Gruber, A. *et al.* Molecular and structural architecture of polyQ aggregates in yeast.
1047   *Proceedings of the National Academy of Sciences* **115**, E3446–E3453 (2018).
1048   42. Chen, M. *et al.* Convolutional neural networks for automated annotation of cellular cryo-
1049   electron tomograms. *Nat. Methods* **14**, 983–985 (2017).
1050   43. Rockabrand, E. *et al.* The first 17 amino acids of Huntingtin modulate its sub-cellular
1051   localization, aggregation and effects on calcium homeostasis. *Hum. Mol. Genet.* **16**, 61–77
1052   (2007).
1053   44. DiGiovanni, L. F., Mocle, A. J., Xia, J. & Truant, R. Huntingtin N17 domain is a reactive oxygen
1054   species sensor regulating huntingtin phosphorylation and localization. *Hum. Mol. Genet.* **25**,
1055   3937–3945 (2016).
1056   45. Steffan, J. S. *et al.* SUMO modification of Huntingtin and Huntington's disease pathology.
1057   *Science* **304**, 100–104 (2004).
1058   46. Maiuri, T., Woloshansky, T., Xia, J. & Truant, R. The huntingtin N17 domain is a
1059   multifunctional CRM1 and Ran-dependent nuclear and cilial export signal. *Hum. Mol. Genet.*
1060   **22**, 1383–1394 (2013).
1061   47. Yano, H. *et al.* Inhibition of mitochondrial protein import by mutant huntingtin. *Nat.*
1062   *Neurosci.* **17**, 822–831 (2014).
1063   48. Yablonska, S. *et al.* Mutant huntingtin disrupts mitochondrial proteostasis by interacting

1064   with TIM23. *Proc. Natl. Acad. Sci. U. S. A.* **116**, 16593–16602 (2019).

1065   49. Pettersen, E. F. *et al.* UCSF ChimeraX: Structure visualization for researchers, educators, and
1066   developers. *Protein Sci.* **30**, 70–82 (2021).

1067   50. Scherzinger, E. *et al.* Huntingtin-encoded polyglutamine expansions form amyloid-like
1068   protein aggregates in vitro and in vivo. *Cell* **90**, 549–558 (1997).

1069   51. Jung, M., Choi, H. & Mun, J. Y. The autophagy research in electron microscopy. *Applied*
1070   *Microscopy* **49**, 1–7 (2019).

1071   52. Zhao, Y. G. & Zhang, H. Autophagosome maturation: An epic journey from the ER to
1072   lysosomes. *J. Cell Biol.* **218**, 757–770 (2019).

1073   53. Wong, Y. C., Ysselstein, D. & Krainc, D. Mitochondria–lysosome contacts regulate
1074   mitochondrial fission via RAB7 GTP hydrolysis. *Nature* vol. 554 382–386 (2018).

1075   54. Johnson, J. *et al.* Mitochondrial dysfunction in the development and progression of
1076   neurodegenerative diseases. *Arch. Biochem. Biophys.* **702**, 108698 (2021).

1077   55. Xavier, V. J. & Martinou, J.-C. RNA Granules in the Mitochondria and Their Organization
1078   under Mitochondrial Stresses. *Int. J. Mol. Sci.* **22**, (2021).

1079   56. Hornig-Do, H.-T. *et al.* Isolation of functional pure mitochondria by superparamagnetic
1080   microbeads. *Anal. Biochem.* **389**, 1–5 (2009).

1081   57. Cherubini, M., Lopez-Molina, L. & Gines, S. Mitochondrial fission in Huntington's disease
1082   mouse striatum disrupts ER-mitochondria contacts leading to disturbances in Ca2+ efflux
1083   and Reactive Oxygen Species (ROS) homeostasis. *Neurobiol. Dis.* **136**, 104741 (2020).

1084   58. Jiang, Y., Chadwick, S. R. & Lajoie, P. Endoplasmic reticulum stress: The cause and solution
1085   to Huntington's disease? *Brain Res.* **1648**, 650–657 (2016).

1086   59. Leitman, J., Ulrich Hartl, F. & Lederkremer, G. Z. Soluble forms of polyQ-expanded huntingtin
1087   rather than large aggregates cause endoplasmic reticulum stress. *Nat. Commun.* **4**, 2753
1088   (2013).

1089   60. Reddy, P. H. Increased mitochondrial fission and neuronal dysfunction in Huntington's
1090   disease: implications for molecular inhibitors of excessive mitochondrial fission. *Drug*
1091   *Discov. Today* **19**, 951–955 (2014).

1092   61. Antonicka, H., Sasarman, F., Nishimura, T., Paupe, V. & Shoubridge, E. A. The mitochondrial
1093   RNA-binding protein GRSF1 localizes to RNA granules and is required for posttranscriptional
1094   mitochondrial gene expression. *Cell Metab.* **17**, 386–398 (2013).

1095   62. Jourdain, A. A. *et al.* GRSF1 regulates RNA processing in mitochondrial RNA granules. *Cell*
1096   *Metab.* **17**, 399–410 (2013).

1097   63. Noh, J. H. *et al.* GRSF1 suppresses cell senescence. *Aging* **10**, 1856–1866 (2018).

1098   64. Jodeiri Farshbaf, M. & Ghaedi, K. Huntington's Disease and Mitochondria. *Neurotox. Res.* **32**,
1099   518–529 (2017).

1100   65. Morozko, E. L. *et al.* PIAS1 modulates striatal transcription, DNA damage repair, and
1101   SUMOylation with relevance to Huntington's disease. *Proc. Natl. Acad. Sci. U. S. A.* **118**,

1102 (2021).

1103 66. Niven, J. E. Neuronal energy consumption: biophysics, efficiency and evolution. *Curr. Opin.*
1104   *Neurobiol.* **41**, 129–135 (2016).

1105 67. O'Rourke, J. G. *et al.* SUMO-2 and PIAS1 modulate insoluble mutant huntingtin protein
1106   accumulation. *Cell Rep.* **4**, 362–375 (2013).

1107 68. Siegmund, S. E. *et al.* Three-Dimensional Analysis of Mitochondrial Crista Ultrastructure in a
1108   Patient with Leigh Syndrome by In Situ Cryoelectron Tomography. *iScience* **6**, 83–91 (2018).

1109 69. Sathasivam, K. *et al.* Identical oligomeric and fibrillar structures captured from the brains of
1110   R6/2 and knock-in mouse models of Huntington's disease. *Human Molecular Genetics* vol.
1111   19 65–78 (2010).

1112 70. Costa, V. *et al.* Mitochondrial fission and cristae disruption increase the response of cell
1113   models of Huntington's disease to apoptotic stimuli. *EMBO Mol. Med.* **2**, 490–503 (2010).

1114 71. Rey, T. *et al.* Mitochondrial RNA granules are fluid condensates positioned by membrane
1115   dynamics. *Nat. Cell Biol.* **22**, 1180–1186 (2020).

1116 72. Website. https://doi.org/10.1016/j.cmet.2013.02.006, doi:10.1016/j.cmet.2013.02.006,.

1117 73. Iborra, F. J., Kimura, H. & Cook, P. R. The functional organization of mitochondrial genomes
1118   in human cells. *BMC Biol.* **2**, 1–14 (2004).

1119 74. Antonicka, H. & Shoubridge, E. A. Mitochondrial RNA Granules Are Centers for
1120   Posttranscriptional RNA Processing and Ribosome Biogenesis. *Cell Rep.* **10**, 920–932 (2015).

1121 75. Noh, J. H. *et al.* HuR and GRSF1 modulate the nuclear export and mitochondrial localization
1122   of the lncRNA RMRP. *Genes Dev.* **30**, 1224–1239 (2016).

1123 76. Martin, J. H. & Matthews, J. L. Mitochondrial granules in chondrocytes. *Calcif. Tissue Res.* **3**,
1124   184–193 (1969).

1125 77. Lehninger, A. L. Mitochondria and calcium ion transport. *Biochem. J* **119**, 129–138 (1970).

1126 78. Strubbe-Rivera, J. O. *et al.* Modeling the Effects of Calcium Overload on Mitochondrial
1127   Ultrastructural Remodeling. *Appl. Sci.* **11**, (2021).

1128 79. Vigont, V. *et al.* Both Orai1 and TRPC1 are Involved in Excessive Store-Operated Calcium
1129   Entry in Striatal Neurons Expressing Mutant Huntingtin Exon 1. *Front. Physiol.* **6**, 337 (2015).

1130 80. Kolobkova, Y. A., Vigont, V. A., Shalygin, A. V. & Kaznacheyeva, E. V. Huntington's Disease:
1131   Calcium Dyshomeostasis and Pathology Models. *Acta Naturae* **9**, 34–46 (2017).

1132 81. Panov, A. V. *et al.* Early mitochondrial calcium defects in Huntington's disease are a direct
1133   effect of polyglutamines. *Nat. Neurosci.* **5**, 731–736 (2002).

1134 82. Choo, Y. S., Johnson, G. V. W., MacDonald, M., Detloff, P. J. & Lesort, M. Mutant huntingtin
1135   directly increases susceptibility of mitochondria to the calcium-induced permeability
1136   transition and cytochrome c release. *Hum. Mol. Genet.* **13**, 1407–1420 (2004).

1137 83. Angelova, P. R. *et al.* Pharmacological Sequestration of Mitochondrial Calcium Uptake
1138   Protects Neurons Against Glutamate Excitotoxicity. *Mol. Neurobiol.* **56**, 2244–2255 (2019).

1139 84. Estrada Sánchez, A. M., Mejía-Toiber, J. & Massieu, L. Excitotoxic neuronal death and the

1140   pathogenesis of Huntington's disease. *Arch. Med. Res.* **39**, 265–276 (2008).

1141 85.   Deng, J. *et al.* Correlative 3D x-ray fluorescence and ptychographic tomography of frozen-
1142   hydrated green algae. *Sci Adv* **4**, eaau4548 (2018).

1143 86.   Carmo, C., Naia, L., Lopes, C. & Rego, A. C. Mitochondrial Dysfunction in Huntington's
1144   Disease. *Adv. Exp. Med. Biol.* **1049**, 59–83 (2018).

1145 87.   Liu, W., Duan, X., Fang, X., Shang, W. & Tong, C. Mitochondrial protein import regulates
1146   cytosolic protein homeostasis and neuronal integrity. *Autophagy* **14**, 1293–1309 (2018).

1147 88.   Orr, A. L. *et al.* N-terminal mutant huntingtin associates with mitochondria and impairs
1148   mitochondrial trafficking. *J. Neurosci.* **28**, 2783–2792 (2008).

1149 89.   Shirendeb, U. P. *et al.* Mutant huntingtin's interaction with mitochondrial protein Drp1
1150   impairs mitochondrial biogenesis and causes defective axonal transport and synaptic
1151   degeneration in Huntington's disease. *Hum. Mol. Genet.* **21**, 406–420 (2011).

1152 90.   Sunde, M. & Blake, C. The structure of amyloid fibrils by electron microscopy and X-ray
1153   diffraction. *Adv. Protein Chem.* **50**, 123–159 (1997).

1154 91.   Dobson, C. M. The structural basis of protein folding and its links with human disease.
1155   *Philosophical Transactions of the Royal Society of London. Series B: Biological Sciences* vol.
1156   356 133–145 (2001).

1157 92.   Brunk, U. T. & Terman, A. The mitochondrial-lysosomal axis theory of aging: accumulation
1158   of damaged mitochondria as a result of imperfect autophagocytosis. *Eur. J. Biochem.* **269**,
1159   1996–2002 (2002).

1160 93.   Nguyen, M., Sidransky, E. & Westbroek, W. The Deleterious Duo of Neurodegeneration:
1161   Lysosomes and Mitochondria. *Mitochondrial Dysfunction in Neurodegenerative Disorders*
1162   279–300 (2016) doi:10.1007/978-3-319-28637-2_12.

1163 94.   Audano, M., Schneider, A. & Mitro, N. Mitochondria, lysosomes, and dysfunction: their
1164   meaning in neurodegeneration. *J. Neurochem.* **147**, 291–309 (2018).

1165 95.   Wang, Y., Liu, N. & Lu, B. Mechanisms and roles of mitophagy in neurodegenerative diseases.
1166   *CNS Neurosci. Ther.* **25**, 859–875 (2019).

1167 96.   van der Burg, J. M. M. *et al.* Increased metabolism in the R6/2 mouse model of Huntington's
1168   disease. *Neurobiol. Dis.* **29**, 41–51 (2008).

1169 97.   Carroll, J. B., Bates, G. P., Steffan, J., Saft, C. & Tabrizi, S. J. Treating the whole body in
1170   Huntington's disease. *Lancet Neurol.* **14**, 1135–1142 (2015).

1171 98.   Van der Burg, J.M.M., Björkqvist, M. & Brundin P. Beyond the brain: widespread pathology
1172   in Huntington's disease. The Lancet Neurology 8, 765-774 (2009) doi:10.1016/S1474-
1173   4422(09)70178-4.

1174 99.   Paasch, F., den Brave, F., Psakhye, I., Pfander, B. & Jentsch, S. Failed mitochondrial import
1175   and impaired proteostasis trigger SUMOylation of mitochondrial proteins. *J. Biol. Chem.* **293**,
1176   599–609 (2018).

1177 100. Waters, E. *et al.* The SUMO protease SENP3 regulates mitochondrial autophagy mediated

1178   by Fis1. *EMBO Rep.* **23**, e48754 (2022).

1179 101. Lee, Y. H. *et al.* A PIAS1 Protective Variant S510G Delays polyQ Disease Onset by Modifying
1180   Protein Homeostasis. *Mov. Disord.* (2021) doi:10.1002/mds.28896.

1181 102. Chen, X.-Q. *et al.* T-complex protein 1-ring complex enhances retrograde axonal transport
1182   by modulating tau phosphorylation. *Traffic* **19**, 840–853 (2018).

1183 103. Fang, F. *et al.* Synuclein impairs trafficking and signaling of BDNF in a mouse model of
1184   Parkinson's disease. *Sci. Rep.* **7**, 3868 (2017).

1185 104. Zhao, X. *et al.* TRiC subunits enhance BDNF axonal transport and rescue striatal atrophy in
1186   Huntington's disease. *Proc. Natl. Acad. Sci. U. S. A.* **113**, E5655–64 (2016).

1187 105. Fischer, T. D., Dash, P. K., Liu, J. & Waxham, M. N. Morphology of mitochondria in spatially
1188   restricted axons revealed by cryo-electron tomography. *PLoS Biol.* **16**, e2006169 (2018).

1189 106. Mastronarde, D. N. Automated electron microscope tomography using robust prediction of
1190   specimen movements. *J. Struct. Biol.* **152**, 36–51 (2005).

1191 107. Hagen, W. J. H., Wan, W. & Briggs, J. A. G. Implementation of a cryo-electron tomography
1192   tilt-scheme optimized for high resolution subtomogram averaging. *J. Struct. Biol.* **197**, 191–
1193   198 (2017).

1194 108. Zheng, S. Q. *et al.* MotionCor2: anisotropic correction of beam-induced motion for improved
1195   cryo-electron microscopy. *Nat. Methods* **14**, 331–332 (2017).

1196 109. Chen, M. *et al.* A complete data processing workflow for cryo-ET and subtomogram
1197   averaging. *Nat. Methods* **16**, 1161–1168 (2019).

1198 110. Kremer, J. R., Mastronarde, D. N. & McIntosh, J. R. Computer visualization of three-
1199   dimensional image data using IMOD. *J. Struct. Biol.* **116**, 71–76 (1996).

1200 111. Pettersen, E. F. *et al.* UCSF Chimera--a visualization system for exploratory research and
1201   analysis. *J. Comput. Chem.* **25**, 1605–1612 (2004).

1202 112. Çiçek, O., Abdulkadir, A., Lienkamp S. S., Brox T. & Ronneberger O. 3D U-Net: Learning Dense
1203   Volumetric Segmentation from Sparse Annotation. In International conference on medical
1204   image computing and computer-assisted intervention. *Springer, Cham* 424-432 (2016).

1205 113. Cox, J. *et al.* Andromeda: a peptide search engine integrated into the MaxQuant
1206   environment. *J. Proteome Res.* **10**, 1794–1805 (2011).

Supplementary Files

This is a list of supplementary files associated with this preprint. Click to download.

- SupplementiPSandBACHDcryoETmanuscript032622.pdf
- SupplementaryTable3MitochondriaMSdata.xlsx
- reportingsummaryNCOMMS2211340.pdf
- supplementarymovie1q77mitoannotationchimeramovie.mov
- Supplementarymovie2q66hairballannotationchimeramovie.mov